

Department of Physics and Astronomy
University of Heidelberg

Bachelor Thesis in Physics
submitted by

Franziska Sophie Masuch

born in Ostfildern (Germany)

2022

Fluid description of charged hadron production in xenon-xenon collisions at $\sqrt{s_{\text{NN}}} = 5.44 \text{ TeV}$

This bachelor thesis has been carried out by Franziska Sophie Masuch at the
Physics' Institute of Ruprecht Karl University of Heidelberg, Heidelberg (Germany)
under the supervision of
Prof. Dr. Silvia Masciocchi

Abstract

In this thesis characteristics of the quark-gluon plasma emerging in heavy-ion collisions for the special case of xenon-xenon collisions at $\sqrt{s_{NN}} = 5.44$ TeV will be investigated. For that purpose a software package named *FluiduM* is used to simulate the particle spectra of charged hadrons as kaons, pions and protons which are then compared to data from ALICE. The parameters describing the normalisation factor for the initial entropy density ("norm"), the shear viscosity over entropy ratio (η/s), the maximum of the bulk viscosity over entropy ratio ($(\zeta/s)_{\max}$), the time after the collision until the starting time of the hydrodynamic description (τ_0), the kinetic freeze-out temperature (T_{kin}) and the chemical freeze-out temperature (T_{chem}) can be estimated with a grid search. These parameters characterise the evolution and properties of the quark-gluon plasma produced in heavy-ion collisions. It is noticeable that the model calculations of particle spectra cannot describe all data regions equally well and that so for example the charged particle production at high transverse momenta and the charged particle production in semiperipheral collisions are underestimated. This underestimate will be quantified and its impact on the determination of the evolution parameters will be discussed. Finally, an outlook on a possible solution to the problems occurred in this thesis is presented, which is given by the free-streaming approach.

Zusammenfassung

In dieser Arbeit werden Eigenschaften des in Schwerionenkollisionen entstehenden Quark-Gluon-Plasmas speziell für den Fall von Xenon-Xenon-Kollisionen bei $\sqrt{s_{\text{NN}}} = 5.44$ TeV untersucht. Dafür werden von einem Softwarepaket namens FluiduM simulierte Teilchenspektren geladener Hadronen wie Kaonen, Pionen und Protonen mit ALICE Daten verglichen. Mit einer Rastersuche können Abschätzungen über den Normierungsfaktor für die anfängliche Entropiedichte ("norm"), die Scherviskosität über Entropiedichte (η/s), das Maximum der Volumenviskosität über Entropiedichte ($(\zeta/s)_{\text{max}}$), die Zeit nach der Kollision bis zum Beginn der hydrodynamischen Beschreibung (τ_0), die kinetische Freezeout-Temperatur (T_{kin}) und die chemische Freezeout-Temperatur (T_{chem}) getroffen werden, welche die Entwicklung und die Eigenschaften des Quark-Gluon-Plasmas in Schwerionenkollisionen charakterisieren. Es wird beobachtet, dass die Modellrechnung der Teilchenspektren bestimmte Datenbereiche noch nicht ausreichend beschreiben kann und so zum Beispiel die Produktion von geladenen Teilchen bei höheren transversalen Impulsen und die Produktion von geladenen Teilchen in dezentralen Kollisionen unterschätzt. Diese Unterschätzung soll quantifiziert und deren Auswirkung auf die Bestimmung der Evolutionsparameter soll diskutiert werden. Am Ende wird ein Ausblick zu einer möglichen Lösung der aufgetretenen Probleme präsentiert, welche durch den Ansatz des Free-streamings gegeben ist.

Contents

1	Introduction	1
1.1	Standard Model and QCD	1
1.2	Quark-gluon plasma	3
1.3	Evolution of heavy-ion collisions	5
2	ALICE detector and particle spectra	9
2.1	LHC and the ALICE detector	9
2.2	Particle yields and particle spectra	12
2.3	Centrality classes	13
2.4	Data from Xe-Xe collisions	15
3	Theoretical framework for hydrodynamic simulations	18
3.1	Coordinate system	18
3.1.1	Symmetry transformations	20
3.2	Initial conditions by T _R ENT _O	20
3.3	Hydrodynamic evolution in Fluid <u>u</u> M	23
3.3.1	Mode expansion of partial differential evolution equations . . .	23
3.3.2	Transport properties	24
3.4	Calculation of particle spectra with FastReso	25
4	Analysis: Implementation of parameter search	27
4.1	Global fitting procedure	28
4.1.1	Grid search	29
4.2	Comparison to data from Pb-Pb collisions	34
4.3	Variation of the number of centrality classes and p_T -ranges for the fit	36
4.3.1	Four centrality classes and p_T -values up to 3 GeV	36
4.3.2	Four centrality classes and p_T -values up to 2 GeV	39
4.3.3	Five centrality classes and p_T -values up to 2 GeV	41
4.4	Comparison of the different fitting ranges	42

CONTENTS

4.5	Discussion of the thermalisation time and the free-streaming approach	43
5	Summary and Outlook	45
	Bibliography	

Chapter 1

Introduction

In relativistic heavy-ion collisions obtained at the **L**arge **H**adron **C**ollider (LHC) at the European Organisation for Nuclear Research (CERN) a strongly interacting deconfined state of matter of quarks and gluons is formed, called **q**uark-**g**luon **p**lasma (QGP). It is the subject of ALICE, one of the main experiments at CERN, to study these heavy-ion collisions and the quark-gluon plasma. Studying this state of matter is of high interest as this will help understanding the first 10 μs after the Big Bang when the universe was in a similar state. Furthermore, the underlying theory of **q**uantum **c**hromodynamics (QCD), the field theory of the strong interaction, can be investigated.

1.1 Standard Model and QCD

There are four fundamental forces: The strong interaction (carried by gluons), the weak interaction (carried by Z- and W-bosons), the electromagnetic interaction (carried by photons) and the gravitation. Nowadays, our understanding of fundamental forces, except of gravity, is represented in the **S**tandard **M**odel (SM) of particle physics, where the elementary particles and their interactions are described.

As shown in figure 1.1 all already discovered elementary building blocks can be categorised into quarks, leptons and bosons. Additionally, there exist corresponding antiparticles to each quark and lepton, which have the same mass as the original particles, but carry opposite quantum numbers.

The strong interaction is described by QCD. Only particles that carry a property named colour charge can interact via the strong interaction. Those particles are quarks and gluons, also referred to as partons. There are three different colour charges that can be arbitrarily called red, blue and green, respectively antired, antiblue

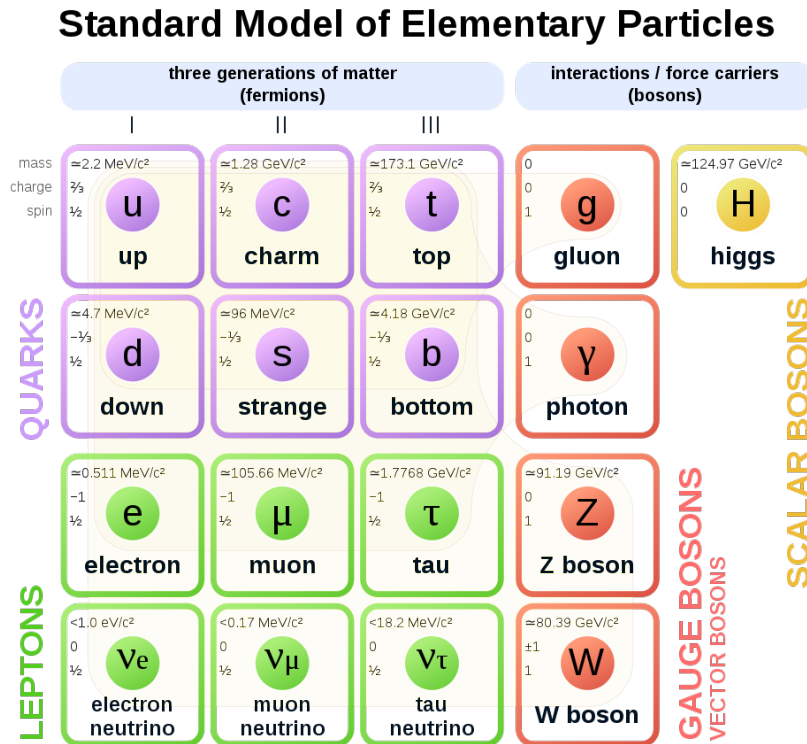


Figure 1.1: Standard model of elementary particles. The elementary building blocks of all matter are given by the 12 fundamental fermions, the "matter particles" (or resp. "antimatter particles"), and 5 fundamental bosons, the "force particles", which are responsible for the interactions between the particles. Figure taken from [1].

and antigreen. Under normal conditions, colour-charged particles can never appear isolated, but must be always bound together with other colour-charged particles into colour-neutral states. This is known as **confinement**. Hence, quarks and gluons are always bound together in colour-neutral hadrons. The most popular examples for hadrons are baryons and mesons. Baryons are made of three quarks with the colours red, blue and green (which together results in a colour-neutral state). Examples for baryons are protons and neutrons.

Mesons on the other side are made of one quark and one antiquark, the possible colour combinations are red+antired, blue+antiblue or green+antigreen. Examples for mesons are pions and kaons.

However, at high energy scales the interactions between quarks and gluons become weaker. This is quantified by the **coupling constant** α_s of QCD. In figure 1.2 the dependency of $\alpha_s(Q^2)$ on the 4-momentum transfer Q^2 is shown. For small values of Q^2 the coupling constant α_s is large and therefore the interactions between quarks

and gluons are strong and confinement prevails. As Q^2 is increasing, the coupling constant α_s asymptotically decreases. The interactions between quarks and gluons become weaker and partons in this regime can therefore move asymptotically freely. For this reason this phenomenon is also called **asymptotic freedom** [2].

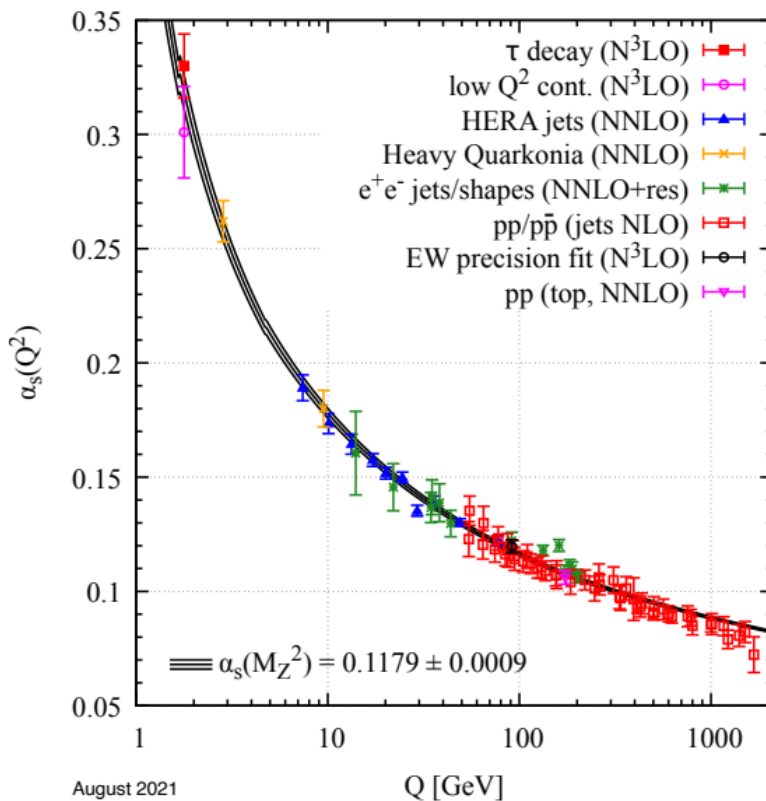


Figure 1.2: Running coupling constant of QCD for the interactions between quarks and gluons in dependence on the momentum transfer Q . The important observation here is that $\alpha_s(Q^2)$ is increasing for $Q \rightarrow 0$ and decreasing for $Q \rightarrow \infty$. Figure taken from [3].

Indeed, the state of deconfinement, when quarks and gluons are not bound together in hadrons anymore but can move quasi-freely, is known as **quark-gluon plasma**.

1.2 Quark-gluon plasma

The quark-gluon plasma is a strongly interacting state of matter that is formed under extremely high energy densities and is composed of deconfined quarks and gluons.

The high energy densities required to form a QGP can be reached in relativistic heavy-ion collisions.

Analogous to the phase diagram of water, in which the different phases like ice, liquid water and vapour can be illustrated in dependency on the pressure and the temperature, there is also a phase diagram for QCD matter (see figure 1.3).

The two relevant thermodynamic potentials in the QCD phase diagram are the

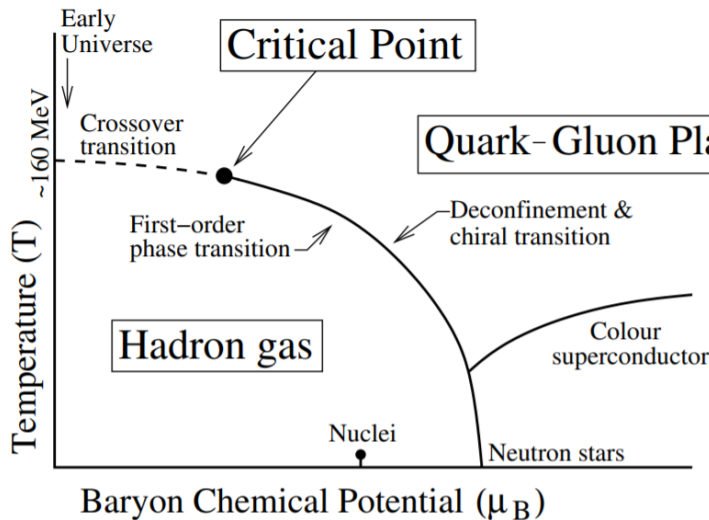


Figure 1.3: The QCD phase diagram. Figure taken from [4].

temperature T , which is on the abscissa, and the baryon chemical potential μ_B , which is on the ordinate. The baryon chemical potential μ_B can be thought of a predominance of quarks over antiquarks in the system. For constant low temperatures, an increasing baryon chemical potential means higher quark densities. Nuclei that make up the ordinary matter we know exist at a temperature close to zero and a baryon chemical potential of $\mu_B \approx 940$ MeV [5]. When μ_B is increasing even further, there is a phase transition into extremely dense matter like it exists in neutron stars.

Let us imagine starting with a hadron gas, so at moderate temperatures and moderate baryon chemical potentials. If this system is heated up, this corresponds to moving vertically upwards in the QCD phase diagram until eventually the energy in the system is high enough and with that the coupling strength α_s for the interactions between quarks and gluons is low enough so that the hadrons deconfine and the state of a quark-gluon plasma is reached.

In the transition between the two phases of a hadron gas and the quark-gluon plasma, there may exist a critical point (see figure 1.3).

The investigation of the different regions of the diagram is very interesting to learn more about QCD. QCD is generally not analytically calculable, but it can be calculated on a grid of points in space and time, the so called lattice QCD, which is under control for small μ_B . Accordingly there are precise predictions for a vanishing baryon chemical potential μ_B (which is related to a vanishing net baryon number density n_B).

It could for example be predicted that the crossover from deconfined QGP to a hadron gas happens for vanishing μ_B at roughly $150 \text{ MeV} - 170 \text{ MeV}$ ¹ [4].

The investigation of the QGP is especially interesting for cosmology and the study of the early universe. Roughly $10 \mu\text{s}$ after the Big Bang, when temperatures were still above 200 MeV , all the matter was still in the state of a QGP [4]. Shortly after the Big Bang, there was almost as much antimatter as matter with only a slight preference for matter over antimatter. Therefore, the baryon chemical potential was close to zero at this time. Consequently, the state of matter in the early universe is located at high temperatures and a low baryon chemical potential in the QCD phase diagram.

As the universe then continued to expand and cool down, the matter could hadronise. The history of the universe with the temperature development over time and the important steps after the Big Bang is shown in figure 1.4. A similar state of matter can be recreated in heavy-ion collisions.

The two most relevant heavy-ion colliders are the **R**elativistic **H**eavy-Ion **C**ollider (RHIC) at the Brookhaven National Laboratory and the **L**arge **H**adron **C**ollider (LHC) at CERN. Understanding the processes in heavy-ion collisions better will also help a lot for a better understanding of QCD matter under extreme conditions.

1.3 Evolution of heavy-ion collisions

The heavy ions are accelerated in the LHC to nearly the speed of light. As a consequence of their ultrarelativistic speed, they are Lorentz contracted in the longitudinal direction. When two of these Lorentz contracted discs collide (or overlap) head-on, the energy and entropy density are so high that many thousands particles are created. Because of the strong interaction among these partons and therefore their collective behaviour, some stages of the evolution can be well described by

¹Remark: Temperature and energy units are related to each other via $E = k_B T$ with the Boltzmann constant $k_B \approx 8.62 \cdot 10^{-5} \text{ eV K}^{-1}$ [5]. An energy of $E = (150 - 170) \text{ MeV}$ would therefore correspond to a temperature of $T = (174 - 197) \cdot 10^9 \text{ K}$. In the following, we will always state the temperature in units of eV resp. MeV.

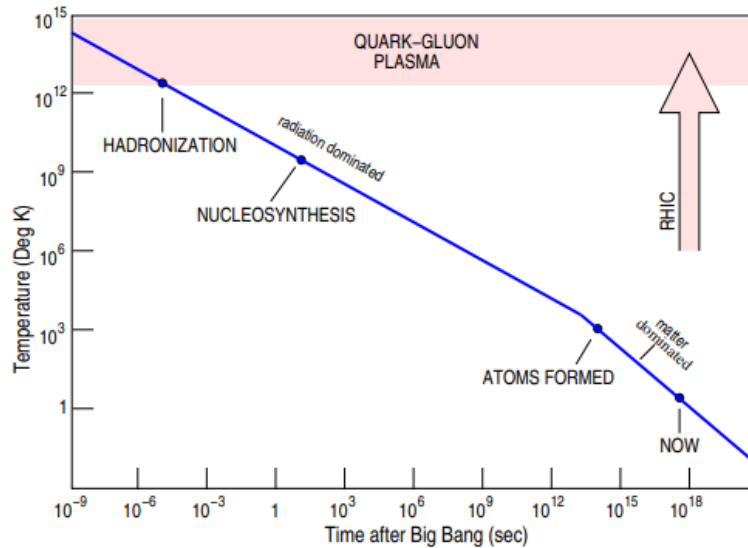


Figure 1.4: Evolution of temperature in the universe. Figure taken from [4].

hydrodynamics. The medium traverses several stages of evolution that are explained in the following.

1. Pre-equilibrium and thermalisation

Shortly after the collision, the created state made of deconfined quarks and gluons is out of equilibrium. Therefore, this stage cannot be described by hydrodynamics yet. A local thermal equilibrium is only reached some time after the collision, called the thermalisation time τ_0 . Typical values for τ_0 lie around $1 \text{ fm}/c$ [4, 38, 39].

2. Quark-gluon plasma phase

After the thermalisation time τ_0 , the state of a quark-gluon plasma is reached. In this phase, the quarks and gluons are in local and thermal equilibrium, therefore they can be described by hydrodynamics. It is important to note that this equilibrium is only local, not global, meaning that equilibrium exists only on small spatial and temporal scales.

3. Hadronisation

As the quark-gluon plasma is expanding, it is cooling down. When the temperature is too low, deconfinement can no longer be maintained and the quarks and gluons form hadrons again. The temperature of hadronisation is called the critical temperature T_c . It lies around $T_c = (156.5 \pm 1.5) \text{ MeV}$ [7, 8].

4. Chemical freeze-out

As the medium continues to cool down, it eventually reaches the chemical freeze-out temperature T_{chem} at which the frequency of inelastic collisions is no longer sufficient

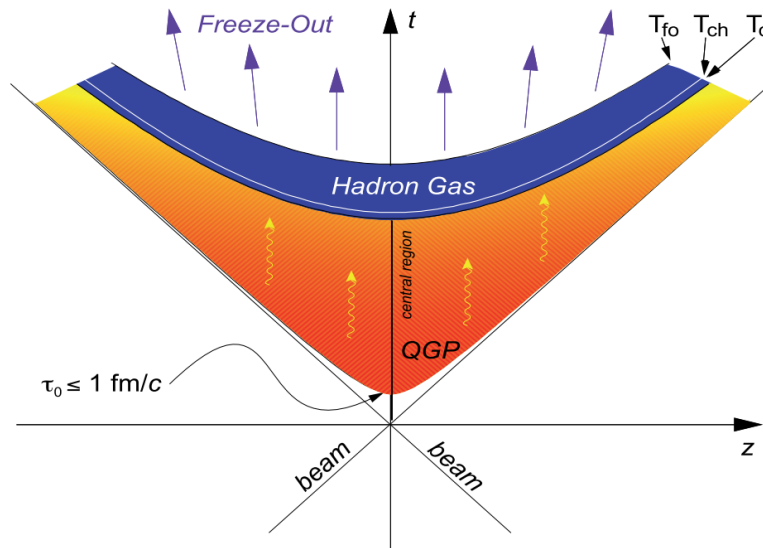


Figure 1.5: Evolution of the quark-gluon plasma in spacetime. As the two reactant nuclei travel at nearly the speed of light before they collide, their projection in spacetime follow the line along $z = \pm t$ with the time coordinate t and the beam direction coordinate z . The interaction point lies at the origin at $t = z = 0$. After the collision, it takes some time until the QGP is formed, this is the thermalisation time τ_0 . The cone then describes the QGP as it is firstly expanding and then freezing out into a hadron gas. Figure taken from [6].

to maintain chemical equilibrium. Typical values for T_{chem} lie around 145 MeV - 150 MeV. The chemical composition of hadron species stays fixed from that time on, except for resonance decays which are still possible.

5. Kinetic freeze-out

At the kinetic freeze-out temperature T_{kin} (or resp. T_{fo} as named in figure 1.5), elastic collisions have become so rare that the hadrons are not able to exchange momentum and energy anymore. That means that the momentum distribution is fixed now.

One needs to remark that the transitions from one stage to the next one are not perfectly sharp, but instead they are continuous. This is illustrated in figure 1.6. But as these crossovers between the different stages of evolution still happen in quite a short time, we will use the simplified assumption of transitions at defined times and temperatures.

The whole evolution from the collision at time $\tau = 0$ fm/c to the thermalisation at $\tau = \tau_0 \approx 1$ fm/c to the freeze-out at $\tau \approx 10$ fm/c happens in a really short time [10, 9, 11]. Compared to these short times, a lot of time passes until the final hadron

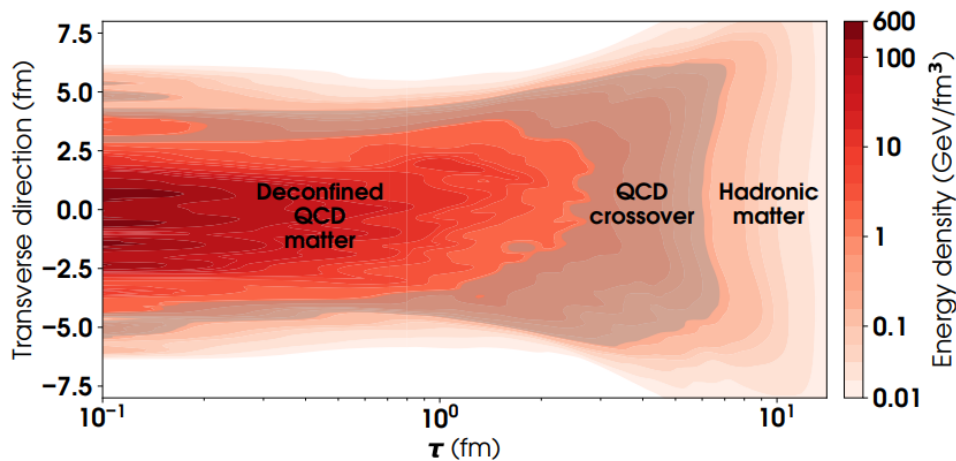


Figure 1.6: Illustration of the energy density in the transverse plane as it is evolving in time. This example represents the energy density in Au-Au collisions at $\sqrt{s_{\text{NN}}} = 200$ GeV. Energy densities for systems of different centre-of-mass collision energies per nucleon-nucleon pair $\sqrt{s_{\text{NN}}}$ and for different ion systems like Pb-Pb or Xe-Xe vary accordingly. The illustration indicates that there is no sharp transition from the quark-gluon plasma to the hadronic matter, but that the transition is continuous. Figure taken from [9].

distributions are measured by the detectors in ALICE at roughly $\tau \approx 10^{15}$ fm/c [10, 11].²

So the QGP exists only on such small temporal and spatial scales that it is not directly accessible by measurements. Only the resulting momentum distributions of particles can be measured and compared to model predictions.

Consequently, we aim at finding a QCD model describing the evolution of a heavy-ion collision and the resulting particle spectra in agreement with the results obtained by the measurements performed in the ALICE detectors.

The data acquisition at ALICE as the experimental part will be introduced in chapter 2 and the theoretical part of the QCD description will be explained in chapter 3.

²As $1 \text{ fm} = 10^{-15} \text{ m}$ and the speed of light is defined to be $c = 299,792,458 \text{ m/s}$ [5], the time of $1 \text{ fm}/c$ measured in seconds is $1 \text{ fm}/c \approx 3.34 \cdot 10^{-24} \text{ s} = 3.34 \text{ ys}$ (yokto seconds) and accordingly $10^{15} \text{ fm}/c \approx 3.34 \cdot 10^{-9} \text{ s} = 3.34 \text{ ns}$ (nano seconds).

Chapter 2

ALICE detector and particle spectra

2.1 LHC and the ALICE detector

The Large Hadron Collider (LHC), with a circumference of 27 kilometres, is the largest and most powerful particle accelerator in the world [12]. It is the main

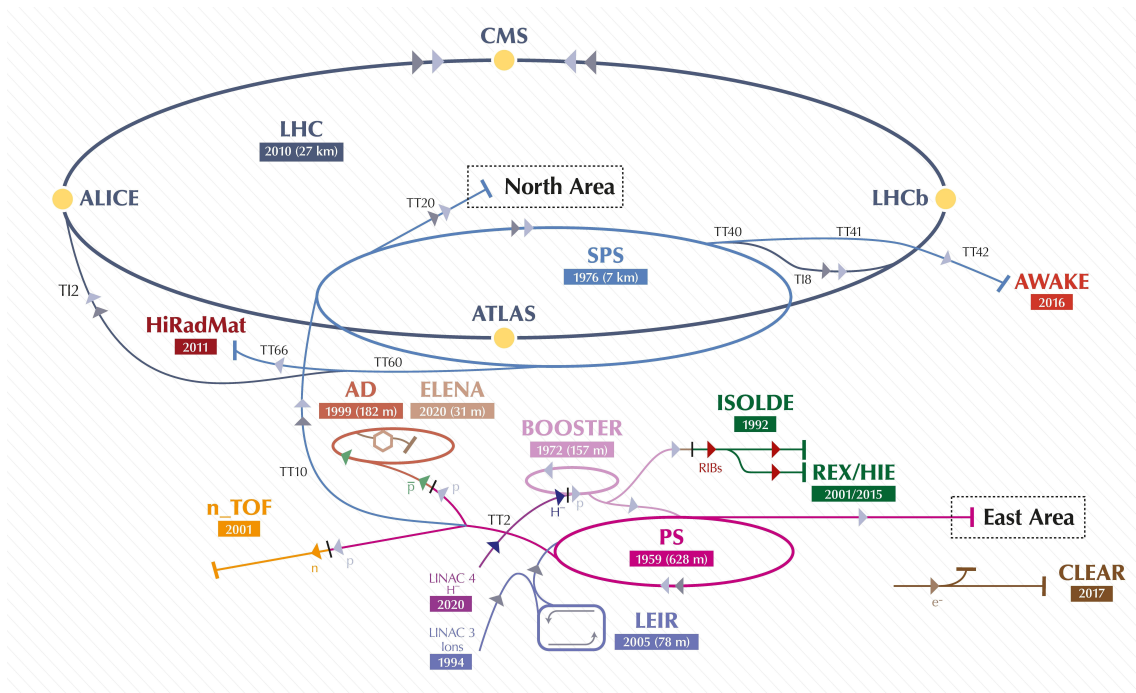


Figure 2.1: The CERN accelerator complex. Figure taken from [13].

accelerator of the European Organisation for Nuclear Research (CERN, from french: Conseil Européen pour la Recherche Nucléaire), which is located near Geneva, at

the border of Switzerland and France.

The LHC is designed as a colliding-beam-accelerator, meaning that particle beams are accelerated into opposing directions until nearly the speed of light and then brought to a frontal collision. The two particle beams travel in separate beam pipes and are made to collide at mainly four different locations, where the experiments ATLAS, CMS, ALICE and LHCb are located [12].

A schematic picture of the CERN accelerator complex with the LHC and its four main experiments together with all the pre-accelerators is shown in figure 2.1.

Most time of the year, proton-proton collisions are realised. Only for roughly one month a year heavier ions like lead-ions are accelerated in the LHC.

Xenon-ions were in fact only injected once and the running time was only one day, which was on the 12th of October 2017 [14].

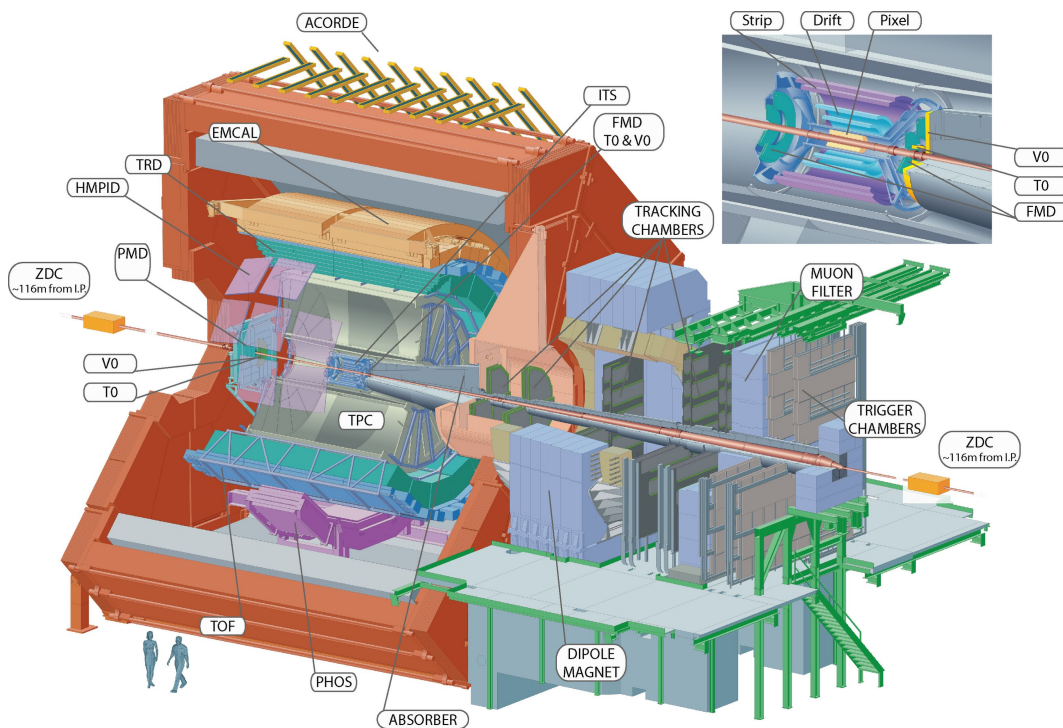


Figure 2.2: Structure of the ALICE detector. Figure taken from [15].

The ALICE detector (acronym for **A** **L**arge **I**on **C**ollider **E**xperiment) is dedicated to study heavy-ion collisions. Its objective is to study strongly interacting matter at extreme energy densities. Figure 2.2 shows a schematic view of the ALICE detector.

The ALICE detector consists of a manifold ensemble of detectors, most of them are located within the large red solenoid magnet. The magnetic field bends the tracks of charged particles, which means that tracing their tracks and their curvature in the detectors allows to determine their charge and momentum. When combining

the information from all detectors, ALICE is able to determine the mass, electrical charge and velocity for particles originated from the collision. To be able to cover a wide momentum range from 0.1 GeV/c up to several GeV/c for thousands of particles per unit of rapidity [16], many different techniques and detectors are used for ALICE, of which the most important ones will be shortly named in the following paragraph. Each of them is covering a different energy and momentum range. This way the combination of all subsystems becomes very strong in particle identification (PID).

Particle identification at ALICE

As already mentioned, ALICE has excellent capabilities to track and identify particles from very low to high transverse momentum p_T .

Starting from the inside (closest to the collision point) to the outside, the **I**nn**T**racking **S**ystem (ITS) is the first sub-detector to name (compare figure 2.2). Its purpose is the identification of charged particles and precise tracking at low momentum and the determination of the primary vertex and secondary decay vertices.

For this, three silicon detectors are used in the ITS: the **S**ilicon **P**ixel **D**etector (SPD), the **S**ilicon **D**rift **D**etector (SDD) and the **S**ilicon **S**trip **D**etector (SSD). The last two perform measurements of the particle momentum and the dE/dx -energy loss by which charged particles can be identified.

Pions and protons up to 0.8 GeV/c can be separated with more than 90% efficiency and a contamination lower than 10%, pions and kaons have a separation efficiency higher than 80% and a contamination lower than 20% [16].

The next detector in line used for PID is the **T**ime **P**rojection **C**hamber (TPC). Just as the ITS, it performs PID at low momenta by an energy loss measurement. But as a large-volume detector filled with a gas-mixture of 90% neon and 10% CO₂, it exploits a different technology. In the gas, three-dimensional reconstructions of the particle trajectories are performed. The 88 cubic meter of gas are contained in a cylinder with an inner radius of 85 cm and an outer radius of 250 cm [16].

The dE/dx -measurements at ITS and TPC are performing well at identification of charged particles at relative low particle's momenta. For intermediate momenta, there is the **T**ime **O**f **F**light module (TOF). The TOF provides PID information in the momentum range from 0.5 GeV/c to 2.5 GeV/c [17]. It is composed of 18 supermodules, each made up itself by five modules, which each contains 15-19 Multigap Resistive Plate Chambers (MRPCs). Each MRPC strip is made of two stacks of resistive glass plates and the gas gaps in between are filled with a gas mixture

of 90% C₂F₄H₂, 5% C₄H₁₀ and 5% SF₆ [16]. Traversing charged particles ionise the gas and the electrons get accelerated towards the anode and cause an electric signal. The traversing particles can be identified by precise time measurements, the TOF has a time resolution better than 50 ps [18].

For the PID capability also for high-momentum ranges the **H**igh-**M**omentum **P**article **I**dentification **D**etector (HMPID) is responsible. The HMPID is a Cherenkov detector [19],[16].

Identification of charged hadrons (like pions, kaons and protons) is well covered with these four different detector systems. For electron identification, there is the **T**ransition **R**adiation **D**etector (TRD) [20] and the **E**lectromagnetic **C**alorimeter (EMCal) [21].

Photons are detected and identified in the **P**hoton **S**pectrometer (PHOS) [22] and muons are triggered and analysed by the muon spectrometer [23].

All sub-detectors together are capable of discriminating the large amount of particles produced in heavy-ion collisions.

For more details on the individual detectors and technologies used for ALICE, see references mentioned above and in special [16] and [24].

2.2 Particle yields and particle spectra

In this thesis transverse-momentum particle spectra will be studied, so the amount of produced charged particles per transverse momentum p_T per collision at midrapidity y in dependence of the p_T -interval¹. Thereby rapidity is defined as

$$y = \frac{1}{2} \cdot \ln \left(\frac{E + p_z c}{E - p_z c} \right), \quad (2.1)$$

where E is the energy, p_z is the component of momentum along the beam axis and midrapidity means values of $|y| < 0.5$, so the rapidity of a particle close to the transverse plane. The measurements are performed at midrapidity.

The particle spectra of the original ALICE data published in [25] are shown in figure 2.3. The figure shows the value of $\frac{1}{N_{ev}} \frac{d^2N}{dp_T dy}$ (N_{ev} is the number of collisions for this measurement) for four different particle species produced in Xe-Xe-collisions: pions, kaons, protons and phi-mesons for p_T -values up to 6 GeV/c.

By integrating the particle spectra over transverse momentum and over rapidity one obtains the integrated particle yield. This quantity measures the overall number

¹ p_T : component of the momentum in the transverse plane.

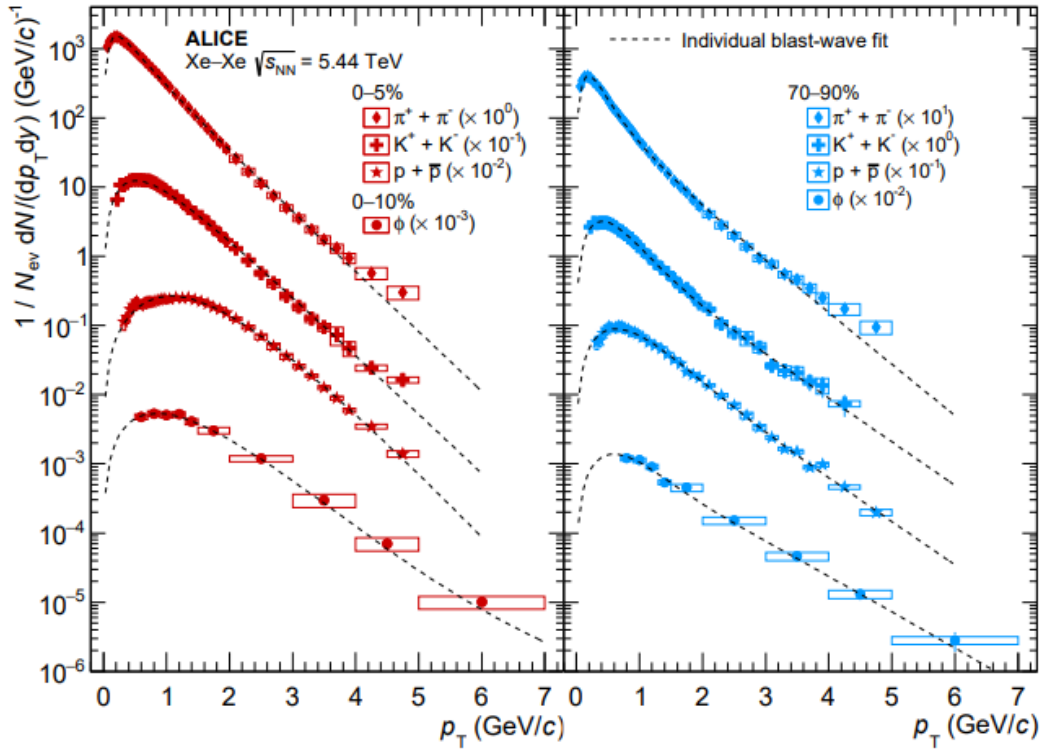


Figure 2.3: Transverse-momentum particle spectra measured by ALICE in Xe-Xe collisions at $\sqrt{s_{NN}} = 5.44$ TeV for pions, kaons, protons and phi-mesons for central collisions (left) and peripheral collisions (right). Statistical uncertainties are shown as error bars and systematic uncertainties are shown as error boxes around the data points. Figure taken from [25].

of produced particles.

2.3 Centrality classes

When two ions collide, it will have a great impact on the subsequent evolution whether the ions hit each other centrally or peripherally. Therefore, we want to have a closer look at the geometry of a heavy-ion collision.

One very important value is the impact parameter b (see figure 2.4), which is the distance between the centres of masses of the two colliding nuclei. An impact parameter of $b = 0$ would refer to perfect central collisions. The larger the value of b , the less central is the collision and the less nucleons will participate in the collision. Hence, the number of participating nucleons N_{part} is correlated to the impact parameter b . In the experiment, the impact parameter b and the number of participating nucleons N_{part} cannot be measured directly. Instead, one correlated quantity, the total number of charged particles measured in the final state N_{ch}

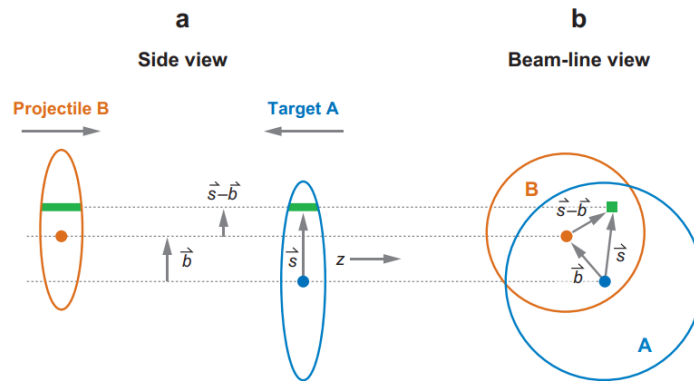


Figure 2.4: Geometry of heavy-ion collisions. Figure taken from [26].

is considered. The most central collisions produce the largest number of charged hadrons. Hence, the impact parameter b , the number of participating nucleons N_{part} and the charged-particle multiplicity N_{ch} are related monotonically to each other. To define centrality classes, the hadronic cross section $\frac{d\sigma}{dN_{\text{ch}}}$ versus multiplicity is measured and segmented into percentiles (see figure 2.5). The 5% that have the highest charged-particle multiplicity N_{ch} are now called the **0-5% centrality class**. The next 5% belong to the 5-10% centrality class, and so on (see figure 2.5).

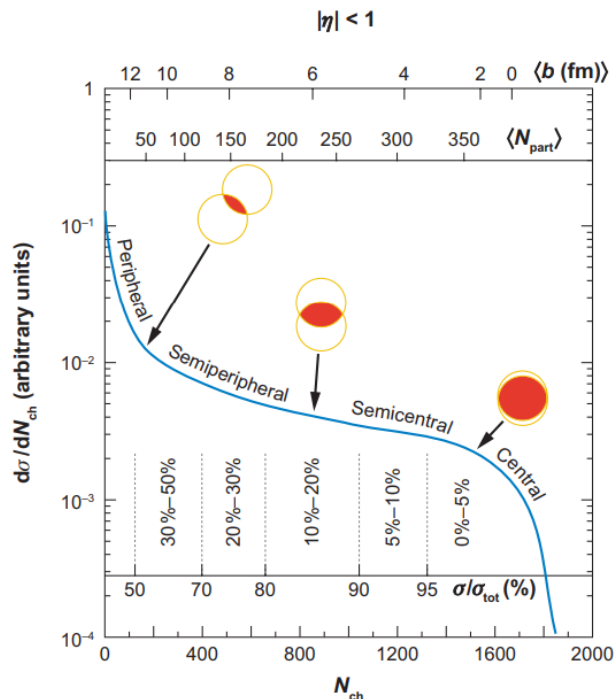


Figure 2.5: Schematic visualisation of centrality classes. Figure taken from [26].

2.4 Data from Xe-Xe collisions

All data that will be used for this analysis can be found and downloaded in [27] and is presented in figure 2.6. It was taken on the 12th of October 2017, when for the first time at LHC Xe-Xe collisions at $\sqrt{s_{NN}} = 5.44$ TeV have been operated.

For pions, kaons and protons, data for the centrality classes 0-5%, 5-10%, 10-20%, 20-30%, 30-40%, 40-50%, 50-60%, 60-70% and 70-90% exist [27].

Figure 2.6 shows the p_T -spectra of π^\pm , K^\pm and p, \bar{p} obtained in the measurements of Xe-Xe collisions at $\sqrt{s_{NN}} = 5.44$ TeV at ALICE for the five most central of the just mentioned centrality classes.

The width of p_T -intervals on the abscissa and the systematic uncertainties in $\frac{1}{N_{ev}} \frac{d^2N}{dp_T dy}$ on the ordinate are indicated by thin error bars. Statistic uncertainties on the measured values on the ordinate are shown as transparent bold error bars. The data from Xe-Xe collisions were taken at a low magnetic field (maximum of $B = 0.5$ T), hence low p_T -ranges are covered by the measurements [25].

The pion measurements (presented in greenish colours in figure 2.6) start at p_T -values of $p_T = (0.065 \pm 0.015)$ GeV/c, the measurements for kaons (indicated in reddish colours) start at $p_T = (0.225 \pm 0.025)$ GeV/c and the ones for protons (in bluish colours) start at $p_T = (0.325 \pm 0.025)$ GeV/c. For all three particle species, data is taken up to $p_T = (4.75 \pm 0.25)$ GeV/c. For each particle species, measurements for five different centrality classes are shown. For each of the three particle species, the curves of the more central events always lie above the less central ones, as evidently more charged particles are produced in central collisions.

Previously, other collision systems, for example pp, p-Pb and Pb-Pb collisions, have already been studied thoroughly. The strongly interacting QGP produced in heavy-ion collisions and its hydrodynamical evolution as well as the hadron production in heavy-ion collisions were therefore quite well known already. Interestingly, it was found that many observations such as the relative abundance of produced hadrons were independent of the collision system and the collision energy, but basically depend only on the final-state multiplicity [25].

Studying Xe-Xe collisions has the potential to fill the gap between p-Pb and Pb-Pb collision systems as xenon has an atomic mass of $m_{Xe} \approx 131$ u and an atomic number of $Z_{Xe} = 54$, therefore one xenon nucleus consists of 54 protons and averagely 77 neutrons. Lead has an atomic mass of $m_{Pb} \approx 207$ u and an atomic number of $Z_{Pb} = 82$, therefore one lead nucleus having 82 protons and averagely 125 neutrons is much heavier and larger than one xenon nucleus [28].

If it is true that the basic principles of the formation and evolution of the QGP

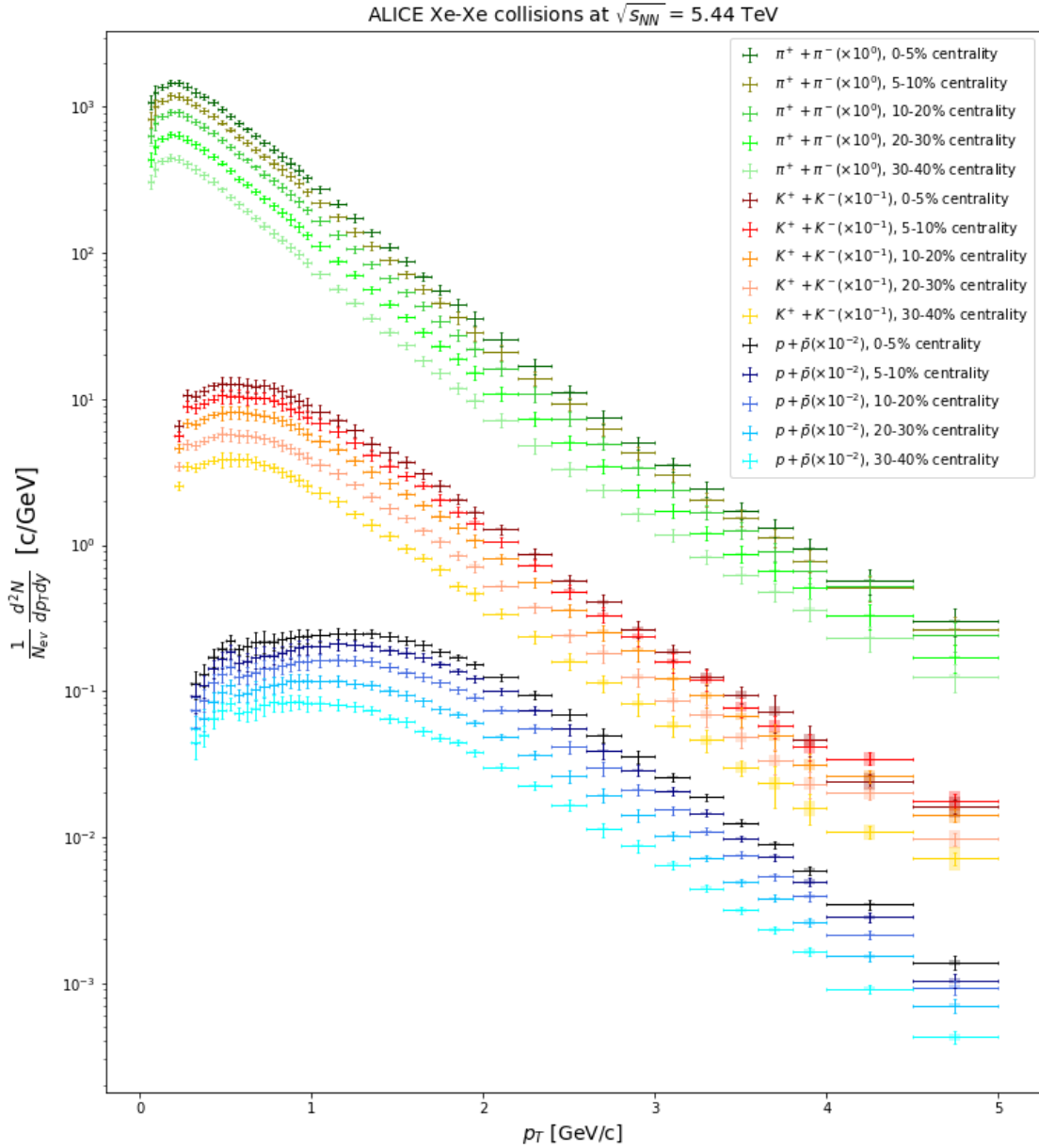


Figure 2.6: Production of $\pi^\pm, K^\pm, p, \bar{p}$ in Xe-Xe collisions at $\sqrt{s_{NN}} = 5.44$ TeV, for each particle species for five centrality classes: 0-5%, 5-10%, 10-20%, 20-30% and 30-40%. For better visibility, pions (in greenish colours) are scaled by 1, kaons (in reddish colours) are scaled by 10^{-1} and the protons (in bluish colours) are scaled by 10^{-2} . The systematic uncertainties in x- and y-direction are shown as thin error bars and the statistical uncertainties in y-direction are shown as transparent, bold error bars. The data for this plot can be found in [27].

are not depending on the collision system, then Xe-Xe collisions should give similar charged-particle spectra as Pb-Pb collisions. Just the multiplicity is expected to be

lower for Xe-Xe than for Pb-Pb collisions as there are less nucleons participating in one collision.

Chapter 3

Theoretical framework for hydrodynamic simulations

As already discussed in chapter 1, the phase of the QGP can be described by fluid dynamics. In our framework, the hydrodynamic description is covered by the software package **FluiduM** (Fluid dynamics of heavy ion collisions with mode expansion) [29].

The initial conditions are provided by **T_RENT_O** (Reduced Thickness Event-by-event Nuclear Topology), which is based on a Monte Carlo Glauber model [30].

After the freeze-out of the QGP and direct decays of resonances, the final particle spectra are calculated with **FastReso** (Fast resonance decays in nuclear collisions) [31].

Each of these three components will be briefly discussed in the following sections. But before introducing a model, we first need to agree on a coordinate system to work in.

3.1 Coordinate system

The origin of our reference frame is set to the collision point, as illustrated in figure 3.1. The z -axis is defined to be coincidental with the beam direction. In a cartesian, right-handed coordinate system, the x - and y -axis are perpendicular to the z -axis, the y -axis is pointing upwards [32]. In the following, the z -direction will be called the longitudinal direction and the x - y -plane will be called the transverse plane. So in cartesian coordinates with the laboratory time t , we use the coordinates (t, x, y, z) to describe points in space and time.

Nevertheless, it is more convenient to transform this to a cylindrical coordinate

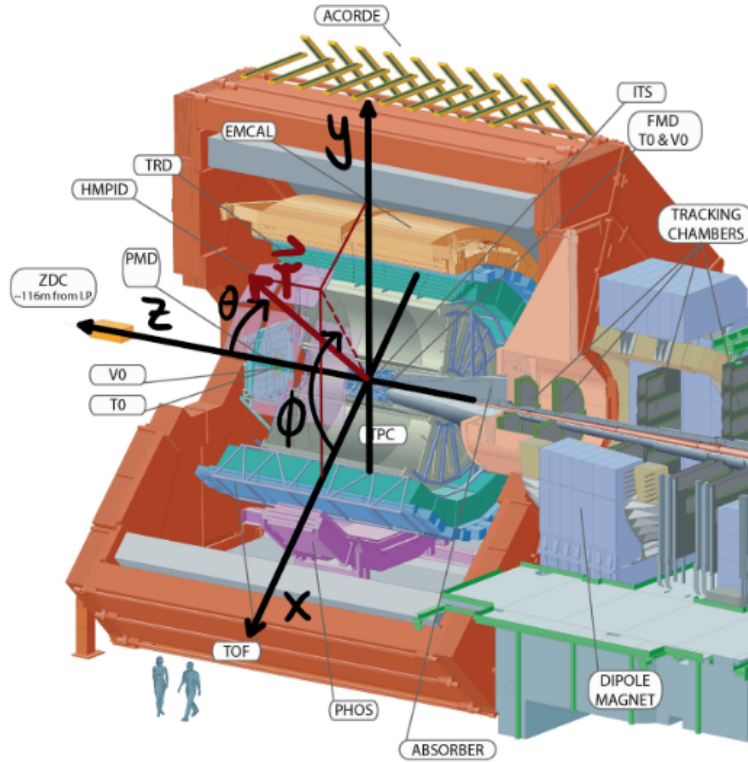


Figure 3.1: Coordinate system in the ALICE experiment. Figure adapted from [15] and inspired by [32].

system with new parametrisations for time and longitudinal direction. We introduce the **Bjorken time** τ , the **radius** r in the transverse plane, the **azimuthal angle** ϕ and the **rapidity** η as follows:

$$\begin{aligned}
 \tau &= \sqrt{t^2 - z^2}, \\
 r &= \sqrt{x^2 + y^2}, \\
 \phi &= \arctan y/x, \\
 \eta &= \operatorname{arctanh} z/t.
 \end{aligned}
 \tag{3.1}$$

The back transformation to the cartesian coordinate system is then given by

$$\begin{aligned}
 t &= \tau \cosh \eta, \\
 x &= r \cos \phi, \\
 y &= r \sin \phi, \\
 z &= \tau \sinh \eta.
 \end{aligned}
 \tag{3.2}$$

3.1.1 Symmetry transformations

The coordinate system described by (τ, r, ϕ, η) is especially useful to approach two symmetry transformations. These are:

1. azimuthal rotations around the beam axis: $\phi \rightarrow \phi + \Delta\phi$
2. rapidity boosts: $\eta \rightarrow \eta + \Delta\eta$.

We will see later in section 3.3 that it is convenient to decompose the fluid fields into an azimuthally symmetric and Bjorken boost invariant background and a fluctuation part.

3.2 Initial conditions by T_RENT_O

For the provision of initial conditions a Monte Carlo Glauber model combined with an entropy production mechanism is used. This is implemented event-by-event in T_RENT_O and then averaged over many events to obtain a transverse entropy density profile at the time of the thermalisation τ_0 of the QGP.

A Glauber model generally describes the collision event of two nuclei A and B as a superposition of collisions of the constituent nucleons. The nuclei A and B can be any nuclei with known number of nucleons n_A and n_B . It is assumed that nucleons can move independently in the nucleus and that they travel on independent linear trajectories when the two nuclei pass through each other. The nuclei are assumed to have a continuous density distribution of nuclear matter participating in inelastic collisions, which is denoted ρ_A^{part} for nucleus A (respectively ρ_B^{part} for nucleus B). The nuclear density distribution is best described by a Woods-Saxon distribution:

$$\rho(r) = \rho_0 \cdot \frac{1 + w(r/R)^2}{1 + e^{(r-R)/a}} \quad (3.3)$$

where ρ_0 is the nuclear density at the centre of the nucleus, w is the deviation from a spherical shape, R is the nuclear radius and a is the skin depth [26].

It is important to note that not all nucleons necessarily participate in the collision and therefore the spectator nucleons have to be excluded from the nuclear density distribution ρ in equation (3.3) to obtain the density distribution of nucleons which are actually participating in the collision ρ^{part} .

In contrast to the optical limit approximation, the Monte Carlo Glauber ansatz assumes discrete positions of each constituent nucleon within the nucleus, which are sampled by a Monte Carlo method according to the nuclear density distribution $\rho(r)$.

Figure 3.2 shows a visualisation for such a Monte Carlo Glauber event in the case of Au-Au collisions. The nucleons of the nucleus A (respectively B) are illustrated by blue (respectively red) dots, whose position is randomly sampled according to (3.3). The nucleons which are participating in the collision are coloured in darker shade, while spectator nucleons are represented by lighter dots.

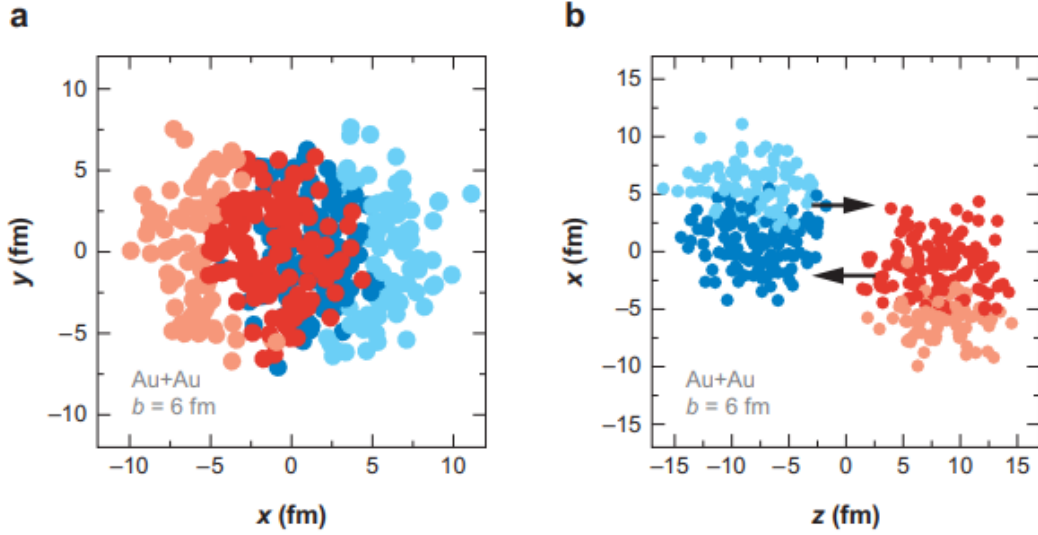


Figure 3.2: Au-Au collision at $\sqrt{s_{\text{NN}}} = 200$ GeV with impact parameter $b = 6$ fm, visualised for one Monte Carlo Glauber event in a) the transverse plane and b) along the beam axis. Participating nucleons in the collision are represented by darker dots while spectator nucleons are represented by lighter dots. Figure taken from [26].

while the spectator nucleons which do not interact and only fly by are represented in lighter shade. With an increasing impact parameter b the number of participating nucleons N_{part} decreases and accordingly the number of spectators N_{spec} rises. The impact parameter b is randomly sampled from the distribution

$$\frac{d\sigma}{db} = 2\pi b \quad (3.4)$$

with the cross section σ [26].

The participating nucleon density distribution $\rho_{A/B}^{\text{part}}$ for the nuclei A and B allows to define the participant thickness function as

$$T_{A/B}(x, y) = \int \rho_{A/B}^{\text{part}}(x, y, z) dz. \quad (3.5)$$

To additionally account for fluctuations and generally for a more detailed explanation, I refer to [33].

In TRENT_O (Reduced Thickness Event-by-event Nuclear Topology) the reduced

thickness function is introduced as

$$T_R(p, T_A, T_B) = \left(\frac{T_A^p + T_B^p}{2} \right)^{1/p} \quad (3.6)$$

with the reduced thickness parameter $p \in \mathbb{R}$.¹

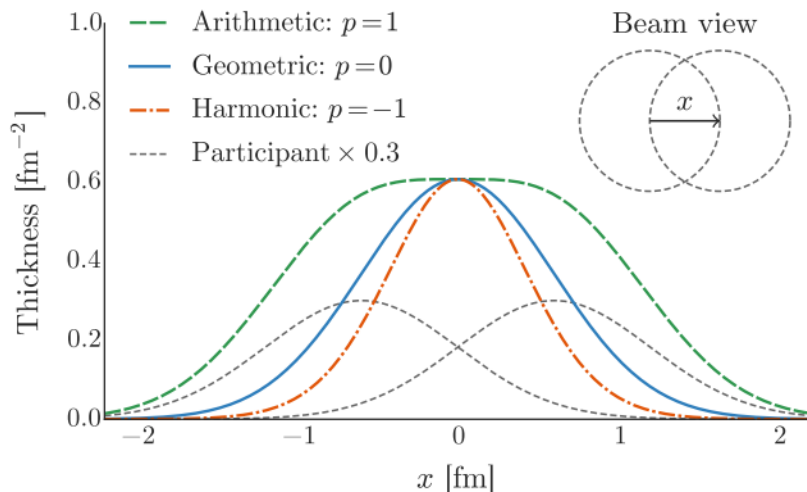


Figure 3.3: Reduced thickness function for a collision of nonzero impact parameter b . The two gray dashed lines represent the participant thickness functions T_A and T_B and the coloured lines show the reduced thickness function T_R for different values of the reduced thickness parameter p . Figure taken from [30].

The shape of the reduced thickness function T_R is shown for different parameters p in figure 3.3.

Because the reduced thickness function is proportional to the entropy density s deposited in the transverse plane at the thermalisation time τ_0 , the parameter p physically corresponds to different entropy production mechanisms as its value affects the shape of T_R . For further elucidations, see [30].

The proportionality between reduced thickness function and entropy density ($T_R \propto s$) is expressed as

$$s(r) = \frac{\text{Norm}}{\tau_0} \langle T_R(r, \phi) \rangle, \quad (3.7)$$

where $\langle T_R(r, \phi) \rangle$ is the reduced thickness function averaged over many thousands of T_RENT_O events.

¹Remark: The formula for the reduced thickness function T_R describes the generalised mean of the thickness functions T_A and T_B , analogous to the reduced mass m_{red} describing the harmonic mean of two masses m_1 and m_2 as $m_{\text{red}} = (m_1^{-1} + m_2^{-1})^{-1}$.

The introduced normalisation constant Norm is a free parameter, which affects the multiplicity of the produced particles.

A deeper introduction to initial conditions and the $\text{T}_{\text{RENT}}\text{O}$ -model is presented in [33]. For further information on the Glauber model, see [26] and for $\text{T}_{\text{RENT}}\text{O}$, see [30].

3.3 Hydrodynamic evolution in FluiduM

FluiduM (Relativistic fluid dynamics with mode expansion) is a software package to solve the equations of relativistic fluid dynamics. This section shall give a brief overview of FluiduM, while a complete introduction can be found in [29].

3.3.1 Mode expansion of partial differential evolution equations

Fluid fields describing the temperature, the fluid velocity, shear stress, bulk viscous pressure and other characteristic fields are collected in the N -dimensional "Nambu spinor" Φ . It is assumed that the fluid evolution can be described by hyperbolic, quasi-linear partial differential equations of the form

$$\mathbf{A}(\Phi, \tau, r) \cdot \partial_\tau \Phi + \mathbf{B}(\Phi, \tau, r) \cdot \partial_r \Phi + \mathbf{C}(\Phi, \tau, r) \cdot \partial_\phi \Phi + \mathbf{D}(\Phi, \tau, r) \cdot \partial_\eta \Phi - \mathbf{S}(\Phi, \tau, r) = 0 \quad (3.8)$$

where $\mathbf{A}, \mathbf{B}, \mathbf{C}, \mathbf{D}$ are $N \times N$ matrices and \mathbf{S} is a N -dimensional vector representing the source term.

FluiduM uses a background-fluctuation splitting to decompose the fluid fields $\Phi(\tau, r, \phi, \eta)$ into an azimuthally symmetric and rapidity boost invariant background $\Phi_0(\tau, r)$ and a rapidity and azimuthally dependent perturbation part $\Phi_1(\tau, r, \phi, \eta)$:

$$\Phi(\tau, r, \phi, \eta) = \Phi_0(\tau, r) + \epsilon \Phi_1(\tau, r, \phi, \eta). \quad (3.9)$$

It is assumed that the fluctuation part is small compared to the background and therefore the fluid fields can be expanded around the background in terms of the expansion parameter ϵ , which is at the end set to $\epsilon \rightarrow 1$.

The expression for Φ in equation (3.9) can then be inserted in the partial differential equations (3.8) and evaluated in orders of ϵ . Considering only terms of zeroth order in ϵ results in the equations of motion for the background fields Φ_0 ; considering only terms of first order in ϵ results in the linearised equations for the perturbations and

taking higher orders of ϵ into consideration reveals quadratic, cubic, and higher mode interactions.

For the equations of motion for the background fields Φ_0 one obtains from (3.8) for zeroth order in ϵ

$$\mathbf{A}_0(\Phi_0, \tau, r) \cdot \partial_\tau \Phi_0(\tau, r) + \mathbf{B}_0(\Phi_0, \tau, r) \cdot \partial_r \Phi_0(\tau, r) - \mathbf{S}_0(\Phi_0, \tau, r) = 0, \quad (3.10)$$

where \mathbf{A}_0 and \mathbf{B}_0 are the new matrices and \mathbf{S}_0 is the new source term vector. Note that the terms in ϕ and η drop out, because the background fields Φ_0 are defined to be symmetric to azimuthal rotations and longitudinal boosts.

For the linearised perturbation equations one obtains

$$\begin{aligned} \mathbf{A}_1(\Phi_0, \tau, r) \cdot \partial_\tau \Phi_1 + \mathbf{B}_1(\Phi_0, \tau, r) \cdot \partial_r \Phi_1 + \mathbf{C}_1(\Phi_0, \tau, r) \cdot \partial_\phi \Phi_1 \\ + \mathbf{D}_1(\Phi_0, \tau, r) \cdot \partial_\eta \Phi_1 - \mathbf{S}_1(\Phi_0, \tau, r) = 0 \end{aligned} \quad (3.11)$$

with the adapted matrices $\mathbf{A}_1, \mathbf{B}_1, \mathbf{C}_1, \mathbf{D}_1$ and the adapted source term vector \mathbf{S}_1 .

By taking the Fourier mode expansion of the perturbation fields

$$\Phi_1(\tau, r, \phi, \eta) = \sum_{m=-\infty}^{\infty} \int \frac{1}{2\pi} e^{im\phi + ik\eta} \tilde{\Phi}_1(\tau, r, m, k) dk \quad (3.12)$$

the linearised perturbation differential equations(3.11) simplify to

$$\begin{aligned} \mathbf{A}_1(\Phi_0, \tau, r) \cdot \partial_\tau \tilde{\Phi}_1 + \mathbf{B}_1(\Phi_0, \tau, r) \cdot \partial_r \tilde{\Phi}_1 + im\mathbf{C}_1(\Phi_0, \tau, r) \cdot \tilde{\Phi}_1 \\ + ik\mathbf{D}_1(\Phi_0, \tau, r) \cdot \tilde{\Phi}_1 - \mathbf{S}_1(\Phi_0, \tau, r) = 0 \end{aligned} \quad (3.13)$$

The equations (3.10) and (3.13) are more convenient, because in contrast to equation (3.8) which depends on τ, r, ϕ and η , so on all four coordinates, the equations (3.10) and (3.13) only depend on the coordinates τ and r . Although these two equations are still non-linear partial differential equations, solving them in two dimensions is easier than solving equations (3.8) in four dimensions.

For more details on this approach, see [29].

3.3.2 Transport properties

There are two viscosities describing the quark-gluon plasma. One is the shear viscosity which counteracts longitudinal movement of fluid parcels, the other one is the bulk viscosity which counteracts radial expansion.

In order to treat them as dimensionless quantities, we will speak about the ratio of

the viscosity over the entropy density s .

The shear viscosity over entropy ratio η/s is assumed to be constant for now. However, approaches for implementing a temperature-dependent η/s have already been made, see for example [11].

In reality η/s should depend on temperature, being large for high temperatures, reaching a minimum around the hadronisation temperature and rising again for lower temperatures [34]. However, by assuming a constant η/s , which then represents an effective averaged value, already good agreement with the experimental data has been achieved [34].

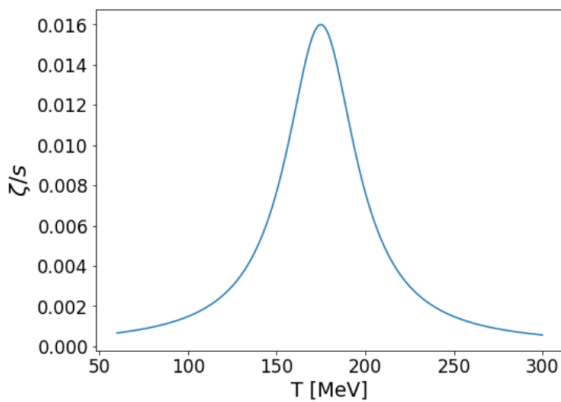


Figure 3.4: Temperature dependence of the bulk viscosity to entropy density ζ/s according to equation (3.14) with $(\zeta/s)_{\max} = 0.016$.

The bulk viscosity over entropy ratio ζ/s is assumed to be temperature-dependent according to a Cauchy distribution

$$\zeta/s = \frac{(\zeta/s)_{\max}}{1 + \left(\frac{T - T_{\text{peak}}}{\Delta T}\right)^2} \quad (3.14)$$

with $T_{\text{peak}} = 175$ MeV and $\Delta T = 24$ MeV [29, 35].

The curve describing this function is shown in figure 3.4.

3.4 Calculation of particle spectra with FastReso

The particle distribution for a particle species a described by $\frac{dN_a}{d^3\mathbf{p}}$ can be calculated by a Cooper-Frye integral over the freeze-out surface Σ :

$$E_{\mathbf{p}} \frac{dN_a}{d^3\mathbf{p}} = \frac{\nu_a}{(2\pi)^3} \int_{\Sigma} f_a(\bar{E}_{\mathbf{p}}) p^\mu d\Sigma_\mu, \quad (3.15)$$

where \mathbf{p} is the momentum and $\bar{E}_{\mathbf{p}} = -u^\nu p_\nu$ the energy in the fluid rest-frame, ν_a is the degeneracy factor of spin or polarisation states and f_a is a particle distribution function [36, 34].

The particle distribution function f_a is given by a Bose-Einstein distribution (for bosons), respectively by a Fermi-Dirac distribution (for fermions), which is

additionally corrected for bulk and shear viscous dissipation:

$$f_a = f_{eq} + \delta f^{bulk} + \delta f^{shear}. \quad (3.16)$$

The Bose-Einstein and Fermi-Dirac distribution functions depend on the energy $\bar{E}_{\mathbf{p}} = -u^\nu p_\nu$, temperature T and the by charge averaged chemical potential μ :

$$f_{eq}(-u^\nu p_\nu, T, \mu) = \frac{1}{e^{-u^\nu p_\nu/T - \mu/T} \mp 1}, \quad (3.17)$$

with the negative sign for Bose-Einstein and the plus sign for Fermi-Dirac statistics [31]. However, since our analysis is performed at LHC energies, we can assume we're working at $\mu = 0$.

After the freeze-out, the particle momentum distribution still changes due to resonance decays. Unstable resonances decay (over several cascades) into relatively stable decay products and thereby add on the distributions of particles like pions, kaons and protons. The calculation of the decays of the unstable resonances is done by the FastReso code.

For more details, I refer to [36] and especially to [31] for a full derivation of the formula for the transverse momentum particle spectra.

In the end, an expression for the resulting particle spectra in the form of $\frac{dN}{2\pi p_T dp_T dy}$ is obtained, which can be evaluated for every particle species of interest and a given set of p_T ranges.

Chapter 4

Analysis: Implementation of parameter search

In this chapter, the procedure for the parameter search will be discussed. With the help of Fluidum, the data presented in figure 2.6 shall be fitted. Fluidum works best for collisions of heavier nuclei and for more central collisions with a large number of participants [36]. Therefore we leave out the peripheral centrality classes in which much less nucleons are participating in the collision and will only consider the centrality classes 0-5%, 5-10%, 10-20%, 20-30% and 30-40% as shown in figure 2.6. We will only look at three different particle types, namely pions, kaons and protons and only at p_T -values up to 3 GeV/c, because fluid dynamics describes only thermal production of particles, meaning particles up to 2 – 3 GeV/c. Particles with higher p_T are produced by other mechanisms that are not included in hydrodynamic models. Therefore p_T -values above 3 GeV/c are excluded in the following from the fitting procedure.

Additionally, previous analyses have already observed that the low-transverse-momentum pions are underestimated in most hydrodynamic simulations like MUSIC or Fluidum [36, 11]. The reason behind this is still under investigation. Anyway, due to this already known observation the low-transverse-momentum pions ($p_T < 0.5$ GeV/c) are also excluded from the fitting procedure.

Furthermore, the output values calculated by Fluidum are multiplied by a factor of $\frac{1}{2\pi p_T}$ compared to the data shown in 2.6 due to a normalisation in spherical coordinates. To allow for a comparison between data values and Fluidum output all data values will be scaled by this factor of $\frac{1}{2\pi p_T}$. Hence, for this analysis the ordinate will be showing values of $\frac{1}{N_{ev}} \frac{1}{2\pi p_T} \frac{d^2 N}{dp_T dy}$ and will therefore be given in units of $\frac{c^2}{GeV^2}$. The abscissa showing the transverse momentum will be given in units of $\frac{GeV}{c}$ (see for

example figure 4.1).

For the input to the Fluidum calculation, a set of six parameters (norm, thermalisation time τ_0 , shear viscosity over entropy ratio η/s , maximum of the bulk viscosity over entropy ratio $(\zeta/s)_{\max}$, kinetic freeze-out temperature T_{kin} and chemical freeze-out temperature T_{chem}) is specified and with that the resulting particle spectra for pions, kaons and protons are calculated.

Unfortunately, no simple function is known that describes the results calculated in Fluidum in dependence on the six input parameters mentioned above. Therefore, each configuration has to be individually computed by Fluidum and compared to the experimental data. As there are six different parameters, a scan with n different values for every dimension would mean a total number of n^6 different configurations. Consequently, the number of different configurations rises quickly with the number of intervals in each dimension (see table 4.1).

n (# intervals in each dimension)	1	2	3	4	5	6	7
n^6 (# configurations)	1	64	729	4,096	15,625	46,656	117,649

Table 4.1: Number of configurations for increasing granularity of the grid.

Despite the fact that the Fluidum calculations of the particle spectra for a single set of parameters are very fast, the grid scans still needed a lot of computational power and were therefore executed on a supercomputer at GSI in Darmstadt.¹ Nevertheless, we limited the grids to six intervals in each dimension, so only coarse grids could be studied in the sixdimensional parameter space.

4.1 Global fitting procedure

To quantify how well the spectra calculation for a specific set of parameters fits to the published ALICE data, the χ^2 -value and the χ^2_{red} -value are calculated:

$$\chi^2 = \sum_{i=1}^N \frac{(x_i - y_i)^2}{\sigma_i^2}$$

$$\chi^2_{\text{red}} = \frac{1}{N_{\text{dof}}} \sum_{i=1}^N \frac{(x_i - y_i)^2}{\sigma_i^2}. \quad (4.1)$$

¹Incidental remark: The "Green Cube" as the huge supercomputer at GSI is called actually deserves to be called "green". It was designed in such a manner that it uses less resources and especially less electricity. It is the most energy-efficient supercomputer all over Europe and the third-most energy-efficient supercomputer worldwide [37].

In these equations, y_i are the spectra-values calculated by Fluidum, x_i are the values of the experimental data and σ_i their corresponding total experimental uncertainties, which are calculated as $\sigma_i = \sqrt{\sigma_{i,\text{stat}}^2 + \sigma_{i,\text{sys}}^2}$, where $\sigma_{i,\text{stat}}$ are the statistical experimental uncertainties and $\sigma_{i,\text{sys}}$ are the systematic experimental uncertainties.

The index i enumerates the different data points whose total number N is the sum of the number of p_T -intervals for each particle type, multiplied with the number of centrality classes. As there are six fitting parameters, the number of degrees of freedom then calculates as $N_{\text{dof}} = N - 6$.

As an example: The first fits were performed to five different centrality classes, each with three different particles, namely pions, kaons and protons. For the pions, we evaluate 25 p_T -values, for the kaons 31 p_T -values and for the protons 29 p_T -values [27]. So all in all, that makes a number of $N = 5 \cdot (25 + 31 + 29) = 425$ different data points that shall be fitted. The number of degrees of freedom would be $N_{\text{dof}} = N - 6 = 425 - 6 = 419$ in this example.

For a good model description, one would expect a value around $\chi_{\text{red}}^2 = 1$. The higher the deviation of the Fluidum output from the data values, the higher the χ_{red}^2 -value and the worse the fit. Therefore, we calculate the χ^2 -value (or respectively the χ_{red}^2 -value) for each gridpoint in the sixdimensional parameter space and then choose that one gridpoint with the lowest χ^2 -value as our best fit. This means that the fitting procedure is a minimisation problem of a sixdimensional surface.

4.1.1 Grid search

The starting ranges of the parameters were setted by following results obtained in previous work [11].

The values for one of the analysed grids are explicitly shown in table 4.2. The grid shown was set up with six equally-spaced intervals in each dimension. So when comparing to table 4.1, this means that this grid includes $6^6 = 46656$ configurations.

norm	0.5	0.7	0.9	1.1	1.3	1.5
η/s	0.28	0.288	0.296	0.304	0.312	0.32
$(\zeta/s)_{\text{max}}$	0.008	0.0096	0.0112	0.0128	0.0144	0.016
τ_0 [fm/c]	$0.5 \cdot 10^{-5}$	$0.8 \cdot 10^{-5}$	$1.1 \cdot 10^{-5}$	$1.4 \cdot 10^{-5}$	$1.7 \cdot 10^{-5}$	$2 \cdot 10^{-5}$
T_{kin} [MeV]	130	132	134	136	138	140
T_{chem} [MeV]	146.5	147	147.5	148	148.5	149

Table 4.2: Parameter ranges for one of the sixdimensional grids.

Of all the possible combinations of the values shown in table 4.2, the following set of parameters results in the lowest χ_{red}^2 -value:

- norm: 1.3
- shear viscosity over entropy ratio η/s : 0.28
- maximum of the bulk viscosity over entropy ratio $(\zeta/s)_{\text{max}}$: 0.0144
- thermalisation time τ_0 : $1.1 \cdot 10^{-5}$ fm/c
- kinetic freeze-out temperature T_{kin} : 136 MeV
- chemical freeze-out temperature T_{chem} : 147.5 MeV

The spectra calculated by Fluidum for these parameters are presented in figure 4.1. When applying equation (4.1), one obtains $\chi^2 = 687.43$. As the number of degrees of freedom is 419, the reduced χ^2 -value is $\chi_{\text{red}}^2 = 1.64$. It was already mentioned that one would usually endeavour to a reduced χ^2 -value around one. As the found value is higher than this, we conclude that the Fluidum calculations are not describing the experimental data very well.

To investigate the possible differences between data and Fluidum output for the best parameter configuration, the ratios between the data measurements and the Fluidum calculation are plotted in figure 4.2. For ratios larger than 1 Fluidum is underestimating the data values and for ratios smaller than 1 it is overestimating them.

It is remarkable that the particles at high p_T in peripheral collisions are significantly underestimated. The ratio for the pions in the 30-40% centrality class reaches up to values higher than two. The more peripheral, the more significant is the deviation.

The kaons in the most central collisions at high p_T -values are overestimated by Fluidum. Therefore they contribute significantly to the χ^2 -value.

By splitting the χ^2 -value into its individual contributions, the values that actually cause the χ^2 -value to be that high can be identified. This confirms the two observations that have already been made (see figure 4.3).

The highest χ^2 -contribution of single p_T -intervals results from the particles produced in peripheral collisions with a high p_T -value, especially the pions. For a reasonable fit, each interval should contribute a value around one on average. But here, the pions reach numbers up to 27, which means that they are not described

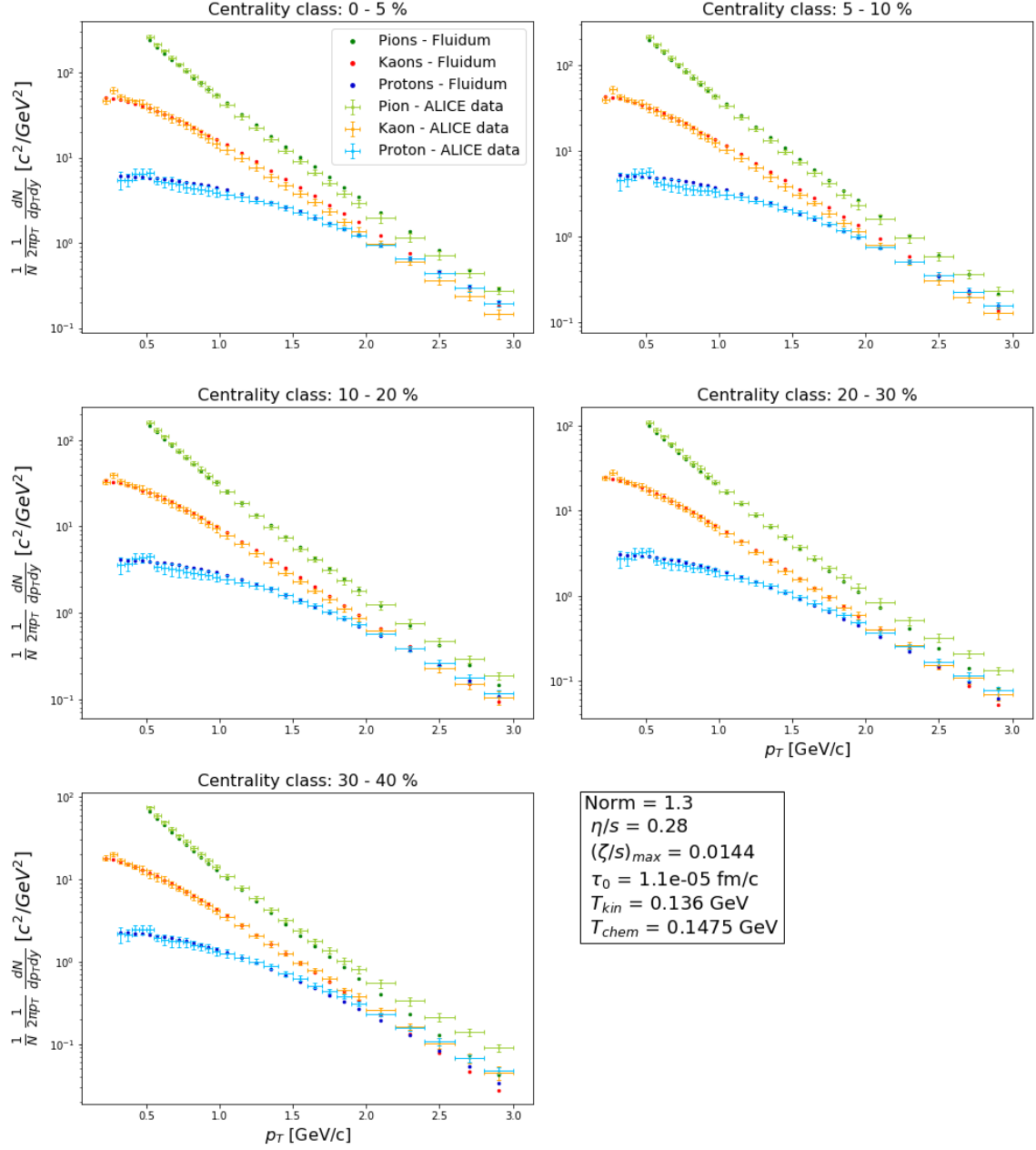


Figure 4.1: p_T -spectra for Xe-Xe collisions at $\sqrt{s_{NN}} = 5.44$ TeV for pions (green), kaons (red) and protons (blue) for the five most central centrality classes. The lighter colours with the indicated errorbars represent the data measurements from ALICE. The dots without errorbars correspond to the output by Fluidum. The parameter input for this specific Fluidum calculation is mentioned in the black-rimmed box. Out of 46656 different possible configurations, these parameters gave the best fitting result. Pions with $p_T < 0.5$ GeV/c have been excluded from the fitting procedure as well as all data for $p_T > 3$ GeV/c and are therefore not plotted here.

well by the Fluidum calculation. Moreover we again see the high- p_T kaons in central collisions as a significant contribution to the total χ^2 -value of the global fit.

4.1. GLOBAL FITTING PROCEDURE

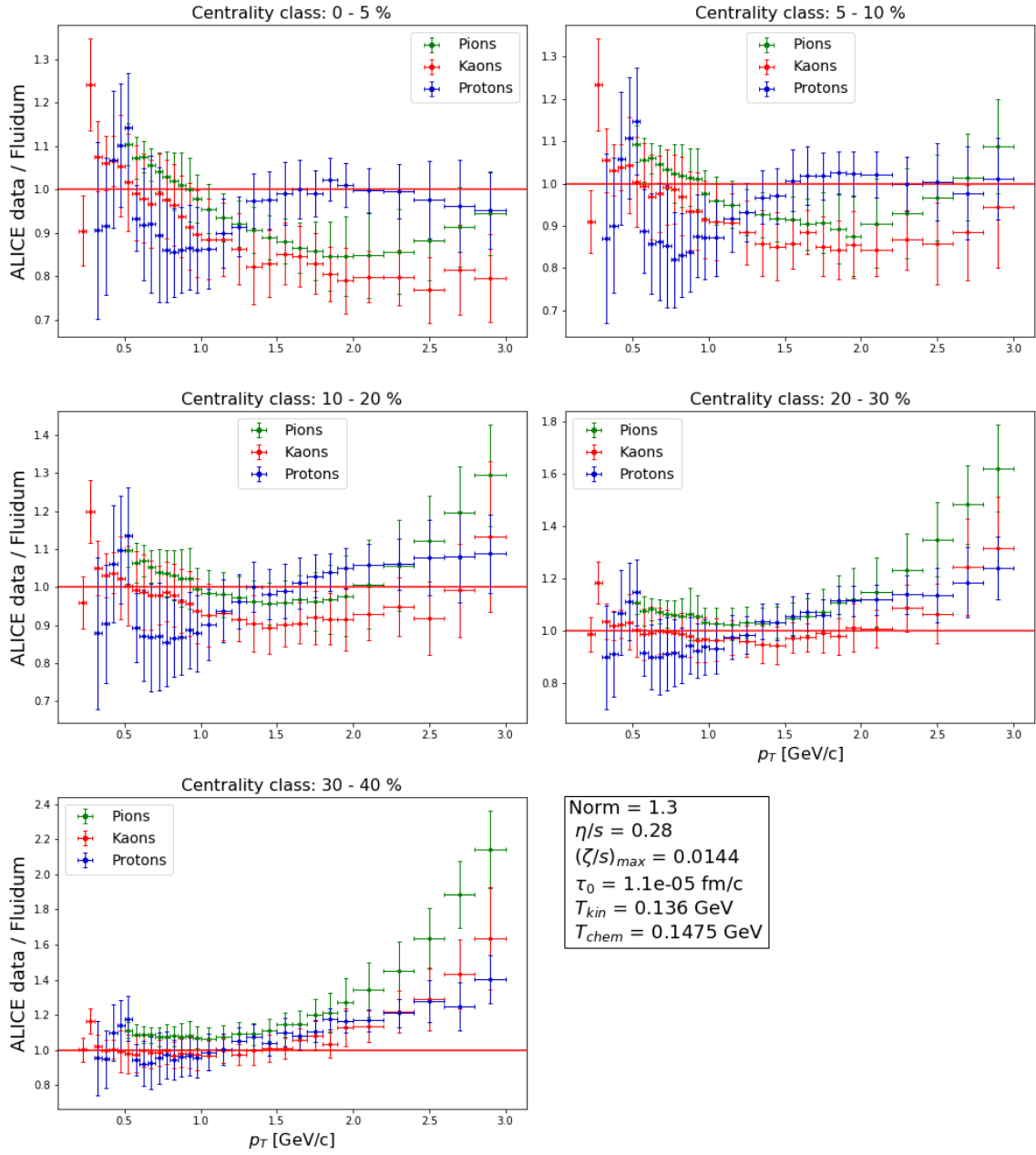


Figure 4.2: Ratio plots for the fit to Xe-Xe data at $\sqrt{s_{NN}} = 5.44$ TeV for five centrality classes and p_T -values up to 3 GeV/c for pions (in green), kaons (in red) and protons (in blue). To better see deviations from the data a red horizontal line at $Y=1$ is shown.

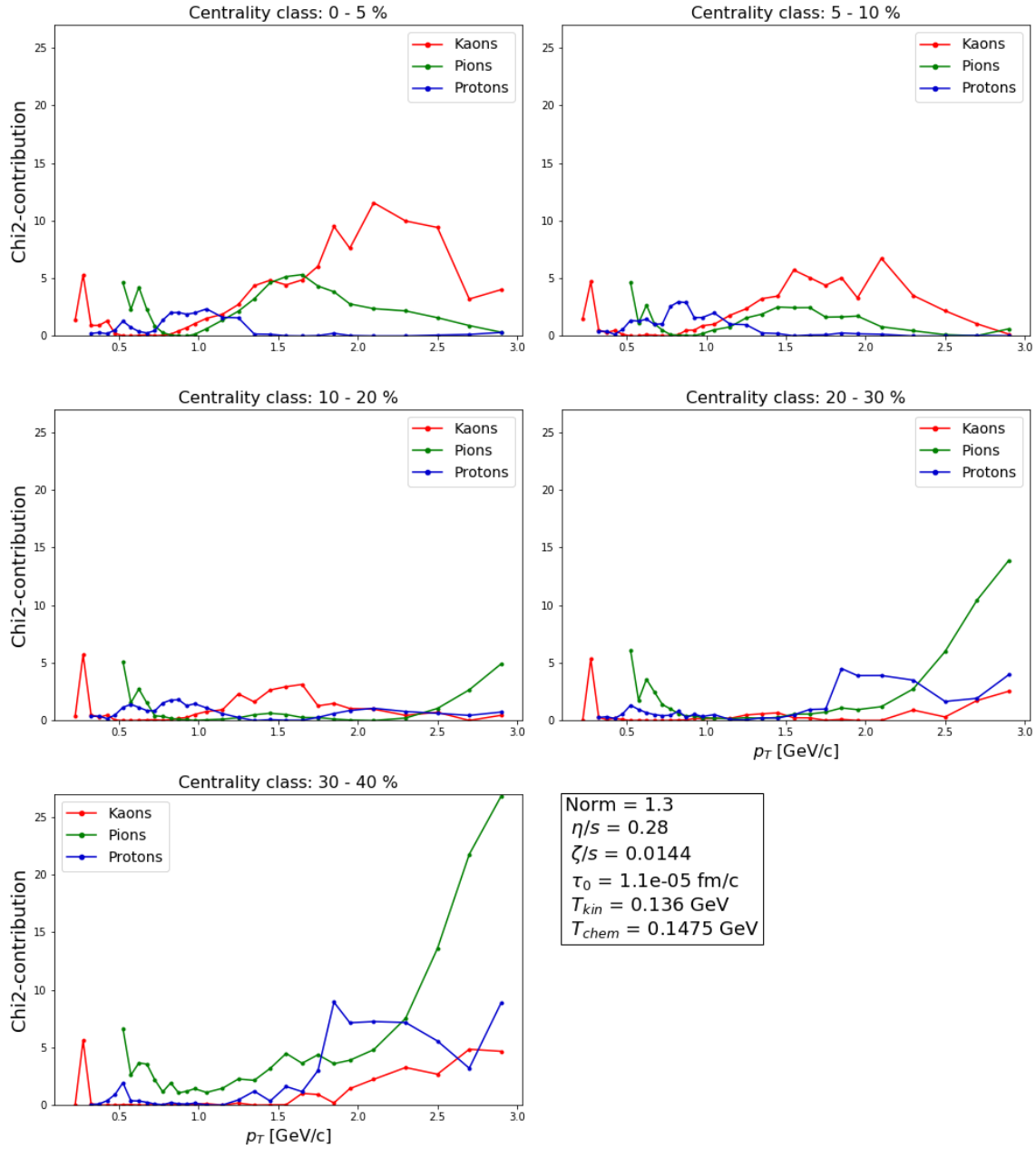


Figure 4.3: Contribution to the χ^2 -value from each p_T -interval for the fit to Xe-Xe data at $\sqrt{s_{NN}} = 5.44$ TeV for five centrality classes and p_T -values up to 3 GeV/c.

By summing the χ^2 -contributions over the p_T -values for the individual particles and the individual centrality classes, the histogram in figure 4.4 is created.

It shows the division of the χ^2 -value into its contributions from the five centrality classes. Within one centrality class, the contributions from the kaons, pions and protons are indicated in red, green and blue.

Comparing the five centrality classes, the 30-40% centrality class contributes the

most to the deviation from unity of the χ^2 -value of the global fit as already observed in figure 4.3. Another significant contribution originates from the kaons in central collisions which again confirms the conclusions drawn from figure 4.3.

The χ^2 -contribution from protons and pions especially in central collisions is low compared to the rest, so protons and pions in central collisions are described well by Fluidum in the global fit.

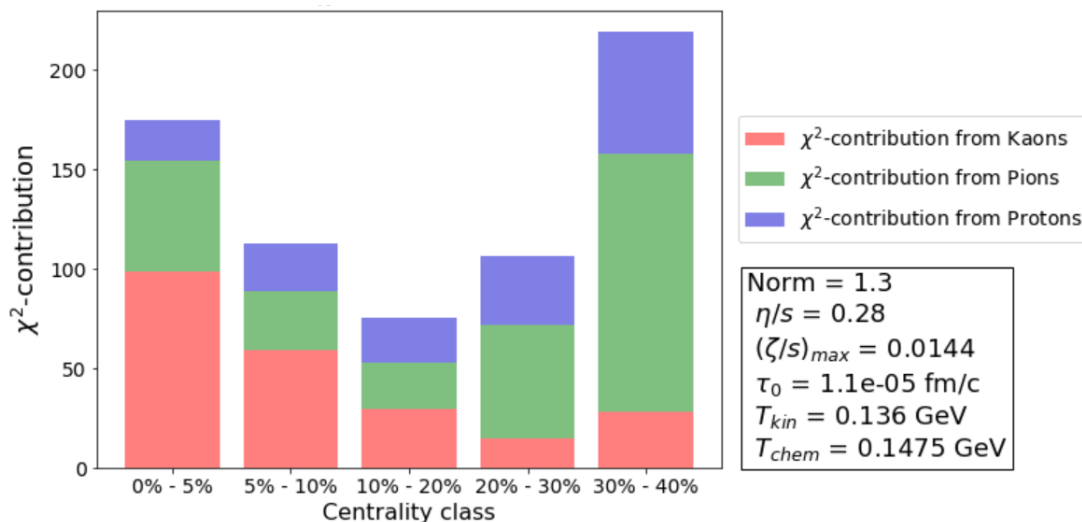


Figure 4.4: Contribution to the χ^2 -value over centrality for the fit to Xe-Xe data at $\sqrt{s_{NN}} = 5.44$ TeV for five centrality classes and p_T -values up to 3 GeV/c.

4.2 Comparison to data from Pb-Pb collisions

In previous analyses for data from Pb-Pb collisions much lower values for the χ_{red}^2 have been found [11], even if the basic settings were similar, for example the centrality intervals analysed, the particle species and their p_T -intervals used in the fitting procedure. Therefore it is important to understand the differences in the results between the Xe-Xe collisions and the Pb-Pb collisions. When looking at equation (4.1) two factors can drive the χ_{red}^2 -value: The difference between the data and the simulation values and secondly the uncertainties on the measurements.

The comparison of the absolute experimental uncertainties of the Xe-Xe and the Pb-Pb measurements for pions, kaons and protons are shown in figure 4.5.

The idea behind comparing the uncertainties of Xe-Xe and Pb-Pb is the following: If the absolute total uncertainties σ_i happened to be much larger for the Pb-Pb dataset, this would result in a smaller χ_{red}^2 -value compared to the Xe-Xe data if the differences between model and data would be of comparable size for both systems.

Figure 4.5 shows the absolute uncertainties in Xe-Xe (dashed lines) and in Pb-Pb (drawn-through lines). For all three particles, pions (in green), kaons (in red) and protons (in blue), the absolute uncertainty is slightly higher for Xe-Xe than for Pb-Pb. So this is definitely not an explanation for the higher χ_{red}^2 in Xe-Xe fits.

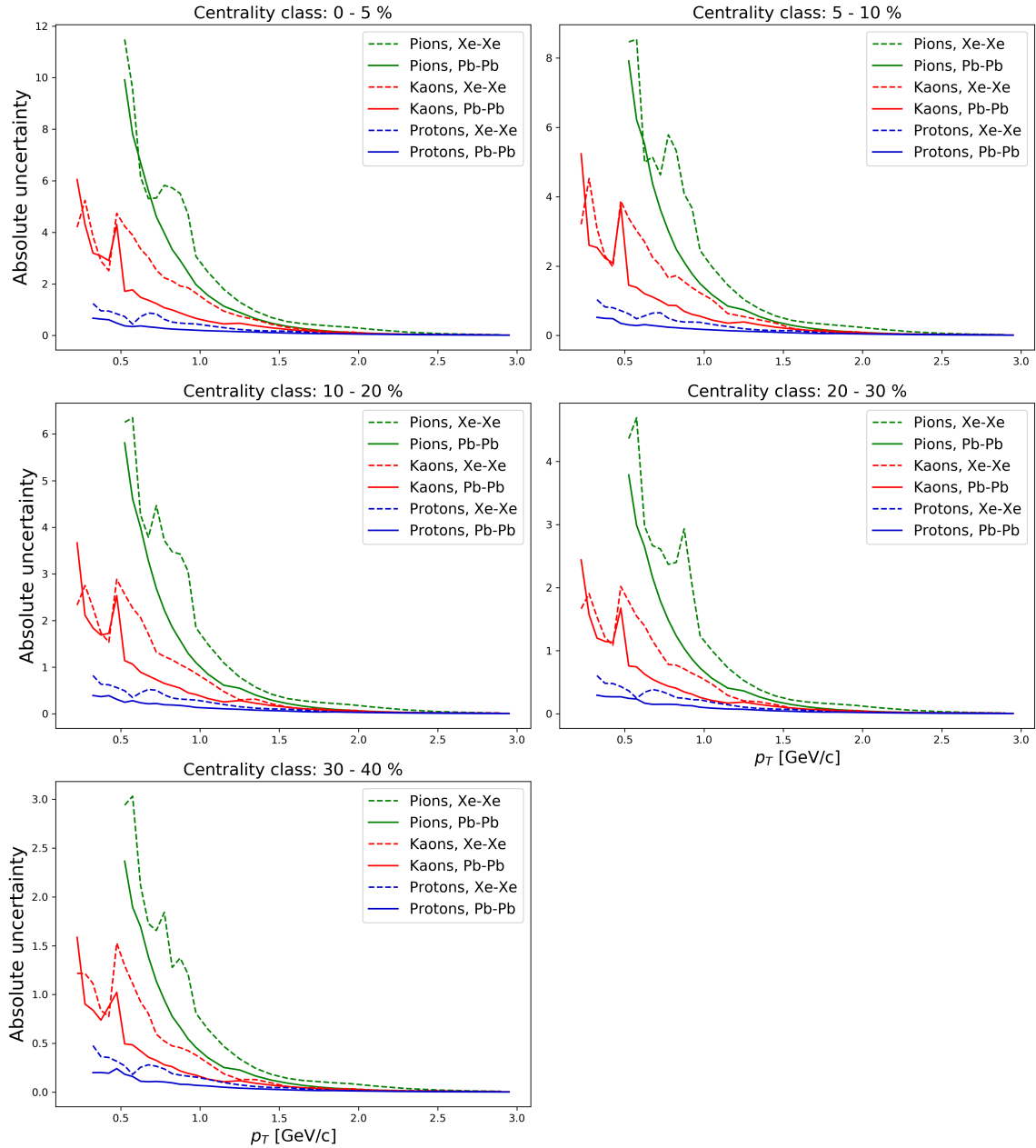


Figure 4.5: Absolute uncertainties of the ALICE data for Pb-Pb- and for Xe-Xe-collisions

4.3 Variation of the number of centrality classes and p_T -ranges for the fit

As presented in figures 4.3 and 4.4 the largest contributions to the χ^2 -value arise mainly from the peripheral centrality classes and from higher p_T -values.

Therefore we want to check whether and how much the fit gets better when excluding these centrality intervals. To make it comparable, the same grid as reported in table 4.2 is used.

4.3.1 Four centrality classes and p_T -values up to 3 GeV

Firstly, only the 30-40% centrality class was excluded from the fit. By recalculating the χ^2 -values, a new gridpoint turned out to result with the lowest χ^2 :

- norm: 1.5
- shear viscosity over entropy ratio η/s : 0.28
- maximum of the bulk viscosity over entropy ratio $(\zeta/s)_{\max}$: 0.016
- thermalisation time τ_0 : $1.7 \cdot 10^{-5}$ fm/c
- kinetic freeze-out temperature T_{kin} : 134 MeV
- chemical freeze-out temperature T_{chem} : 147 MeV

By comparing these values to the ones reported in section 4.1.1, we observe slight variations. The norm increased from 1.3 in the global fit for five centrality classes to 1.5 in the global fit for four centrality classes. Also the thermalisation time τ_0 increased from $1.1 \cdot 10^{-5}$ fm/c to $1.7 \cdot 10^{-5}$ fm/c and the maximum of the bulk viscosity over entropy ratio increased from 0.0144 to 0.016. The two freeze-out temperatures decreased, the kinetic one from 136 MeV to 134 MeV and the chemical one from 147.5 MeV to 147 MeV. The shear viscosity over entropy ratio η/s with a value of 0.28 stayed unchanged.

At this point no error estimation has been done yet, therefore it can't be evaluated if these deviations are significant or not. But we can observe for example, that the norm and the thermalisation time τ_0 have increased simultaneously, which could be explained by equation (3.7), where the factor $\frac{Norm}{\tau_0}$ comes in and explains a positive correlation between Norm and τ_0 .

When calculating the χ^2 -value according to equation (4.1), this results to be $\chi^2 = 445.16$ and when taking the number of degrees of freedom of $N_{\text{dof}} = 334$ into consideration, the reduced χ^2 turns out to be $\chi_{\text{red}}^2 = 1.33$. This is lower than the value of $\chi_{\text{red}}^2 = 1.64$ that was calculated for five centrality classes.

One conclusion that could be drawn is that Fluidium is describing the more central collisions better than the peripheral ones. To further evaluate the new global fit for

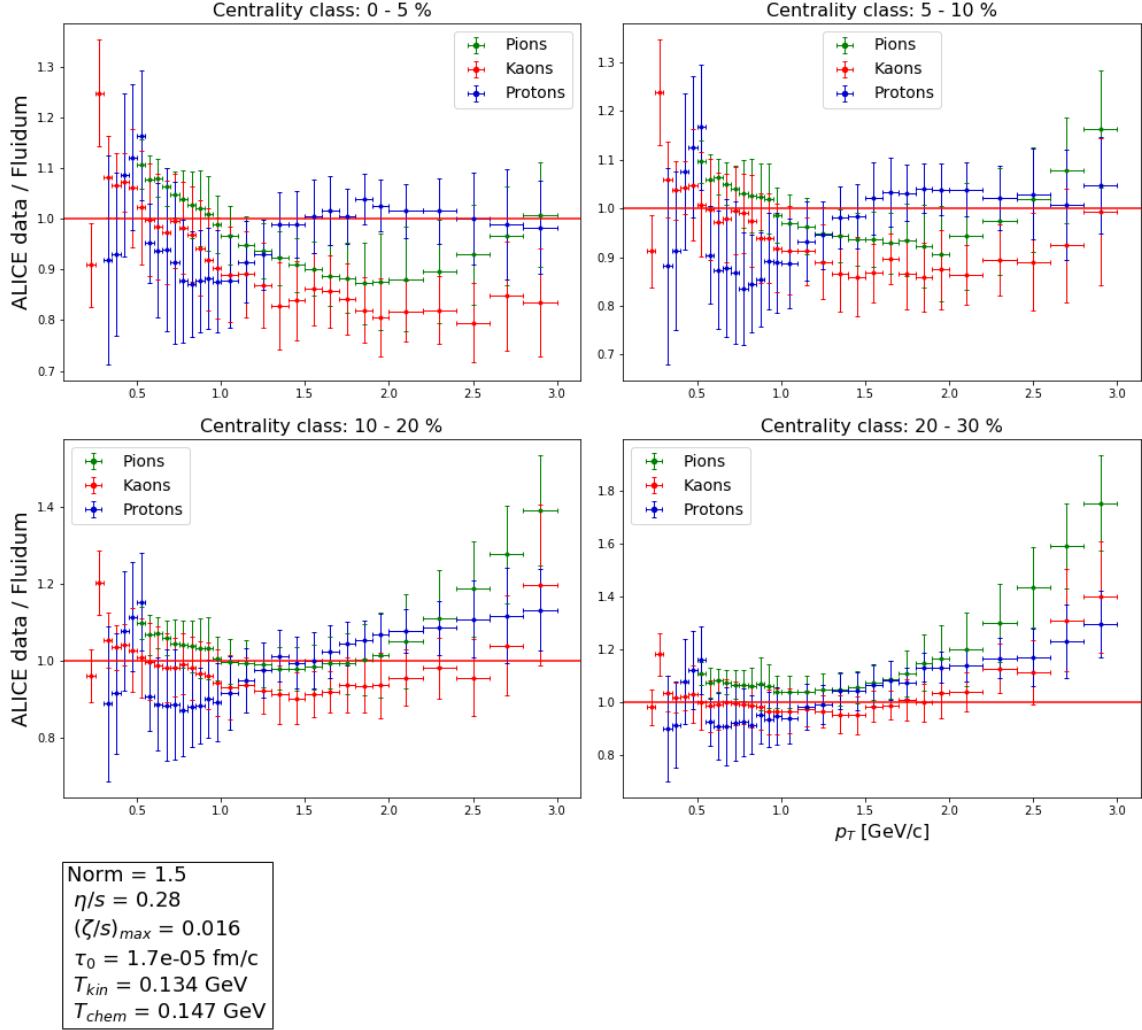


Figure 4.6: Ratio plots for the global fit to Xe-Xe data at $\sqrt{s_{\text{NN}}} = 5.44 \text{ TeV}$ for four centrality classes and p_T -values up to 3 GeV/c for pions (in green), kaons (in red) and protons (in blue). To better see deviations from the data a red horizontal line at $Y=1$ is shown.

four centrality classes, the data-to-model ratios are plotted in figure 4.6 and can be compared to the ratio plots in figure 4.2. We see that the ratios in the first four centrality classes (0-5%, 5-10%, 10-20%, 20-30%) are very similar in both cases.

4.3. VARIATION OF THE NUMBER OF CENTRALITY CLASSES AND P_T -RANGES FOR THE FIT

The data-to-model ratio for the kaons in the 0-5% centrality class for high p_T lies around 0.8 ± 0.1 in both global fits, which means that the high- p_T kaons in central collisions are equally overestimated in both cases.

The ratio for the pions in the 20-30% centrality class rises up to 1.62 ± 0.17 in figure 4.2, while in figure 4.6 it rises up to 1.75 ± 0.18 for $p_T = (2.9 \pm 0.1)$ GeV/c. As these two ranges overlap with each other, but by far not with the optimal ratio value of 1, the exclusion of the 30-40% centrality class in the global fitting procedure did not achieve a significant improvement of the fit for the high- p_T pions in semiperipheral collisions.

As the ranges for the data-to-model ratios don't overlap with the value of 1 for many data points, it can be concluded that the model is not describing the data well and that the exclusion of the 30-40% centrality class did not achieve a significant improvement.

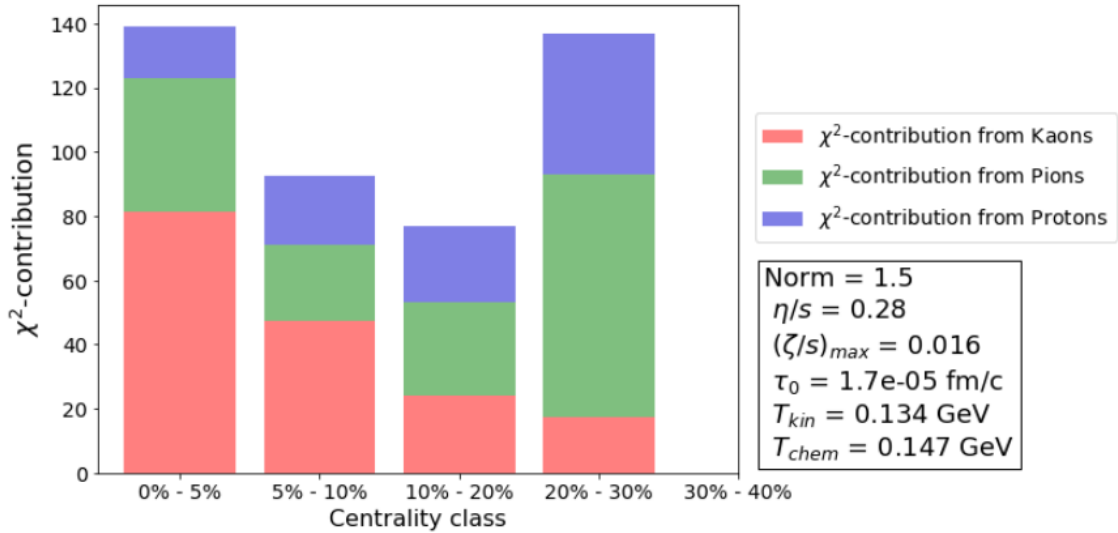


Figure 4.7: Contribution to the χ^2 -value over centrality for the global fit to Xe-Xe data at $\sqrt{s_{NN}} = 5.44$ TeV for four centrality classes and p_T -values up to 3 GeV/c.

This can be even further investigated by comparing the accumulated χ^2 -contributions for the first four centrality classes. As already mentioned, in the global fit to four centrality classes described in this section a total χ^2 -value of 455.16 is obtained. The allocation of the total χ^2 to the single centrality classes is presented in figure 4.7. By comparing this plot to the one in figure 4.4, we observe that indeed the χ^2 -contribution decreases for the 0-5% centrality class from 174 in figure 4.4 to 139 in figure 4.7 and it decreases as well for the 5-10% centrality class from 113 to 93. But on the other hand, the χ^2 -contribution in the 10-20% centrality class increased

slightly from 75 to 77 and in the 20-30% centrality class from 106 to 137, so that altogether the first four centrality classes make up an amount of 469 of the total χ^2 in the global fit performed to five centrality classes and p_T -values up to 3 GeV/c. The χ^2 -value for the global fit to four centrality classes and p_T -values up to 3 GeV/c is with a value of 455 not significantly lower. So up to this point it has been pointed out that the 30-40% centrality class is not described well by the model, but also by excluding the 30-40% centrality class from the fit the given data cannot be described significantly better. Therefore it can be concluded that there are more effects that our model is not describing properly.

4.3.2 Four centrality classes and p_T -values up to 2 GeV

Not just the peripheral centrality classes, but also the high p_T -intervals reduce significantly the goodness of the fit. Therefore the fit was redone for four centrality classes (0-5%, 5-10%, 10-20% and 20-30%) and p_T -values only up to 2 GeV/c.

The following parameters were identified to provide the lowest χ^2 :

- norm: 1.1
- shear viscosity over entropy ratio η/s : 0.28
- maximum of the bulk viscosity over entropy ratio $(\zeta/s)_{\max}$: 0.016
- thermalisation time τ_0 : $1.1 \cdot 10^{-5}$ fm/c
- kinetic freeze-out temperature T_{kin} : 130 MeV
- chemical freeze-out temperature T_{chem} : 147 MeV

Compared to the values found in section 4.3.1, where the global fit was performed to four centrality classes but p_T -values were included up to 3 GeV/c, the values norm, τ_0 and T_{kin} have decreased. With a $\chi^2 = 308.24$ at a number of degrees of freedom of 274, the resulting $\chi_{\text{red}}^2 = 1.12$ is already getting quite close to a value of 1. This means that by excluding the 30-40% centrality class and p_T -values above 2 GeV/c, the goodness of the fit of Fluidum values to actual data is getting quite well.

This can as well be seen in figure 4.8, where the data-to-model ratios for the fit to four centrality classes and p_T -values up to 2 GeV/c are plotted. Compared to the previous ratio plots in figure 4.2 and figure 4.6, most ratios now lie around unity. We also see the improvement of the fit by looking at the χ^2 -contributions for each p_T -value, which are plotted in figure 4.9.

4.3. VARIATION OF THE NUMBER OF CENTRALITY CLASSES AND P_T -RANGES FOR THE FIT

The χ^2 -contribution per data point rises to a maximum of 6 in this case, whereas in figure 4.3 in the fit with five centrality classes and p_T -values up to 3 GeV/c a χ^2 -contribution up to 27 was reached.

Nevertheless, as already mentioned, in an optimal fit all χ^2 -contributions per data point should be close to unity. But in figure 4.9 we rather see that many data points seem to be described very closely by the model as their χ^2 -contribution is close to zero, for example for pions and protons in the 5-10% and in the 10-20% centrality class at p_T around 1 GeV/c, while some outliers increase the total χ^2 with higher contributions, especially kaons in the 0-5% centrality class and high- p_T pions and protons in the 20-30% centrality class.

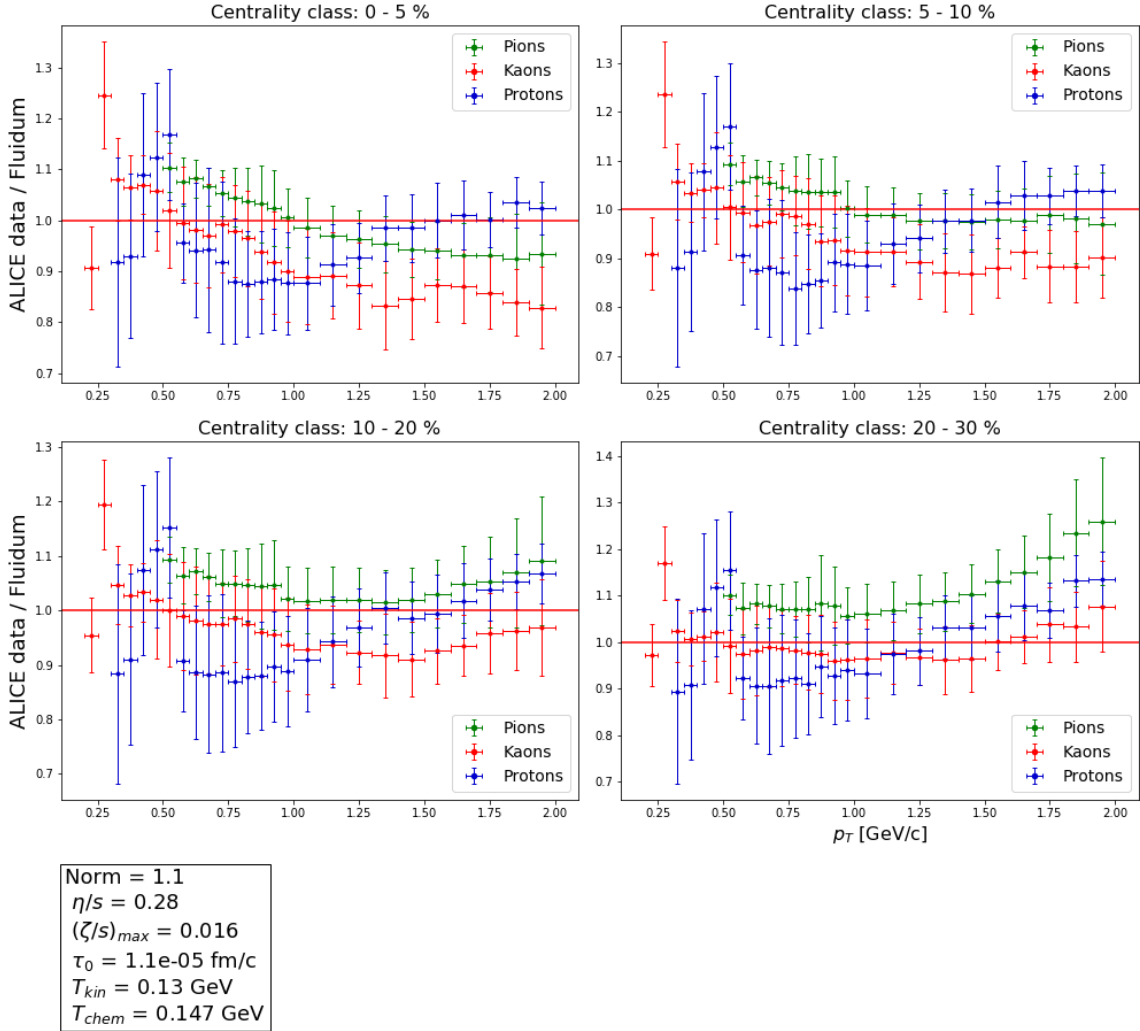


Figure 4.8: Ratio plots for the fit to Xe-Xe data at $\sqrt{s_{NN}} = 5.44 \text{ TeV}$ for four centrality classes and p_T -values up to 2 GeV/c. To better see deviations from the data a red horizontal line at $Y=1$ is shown.

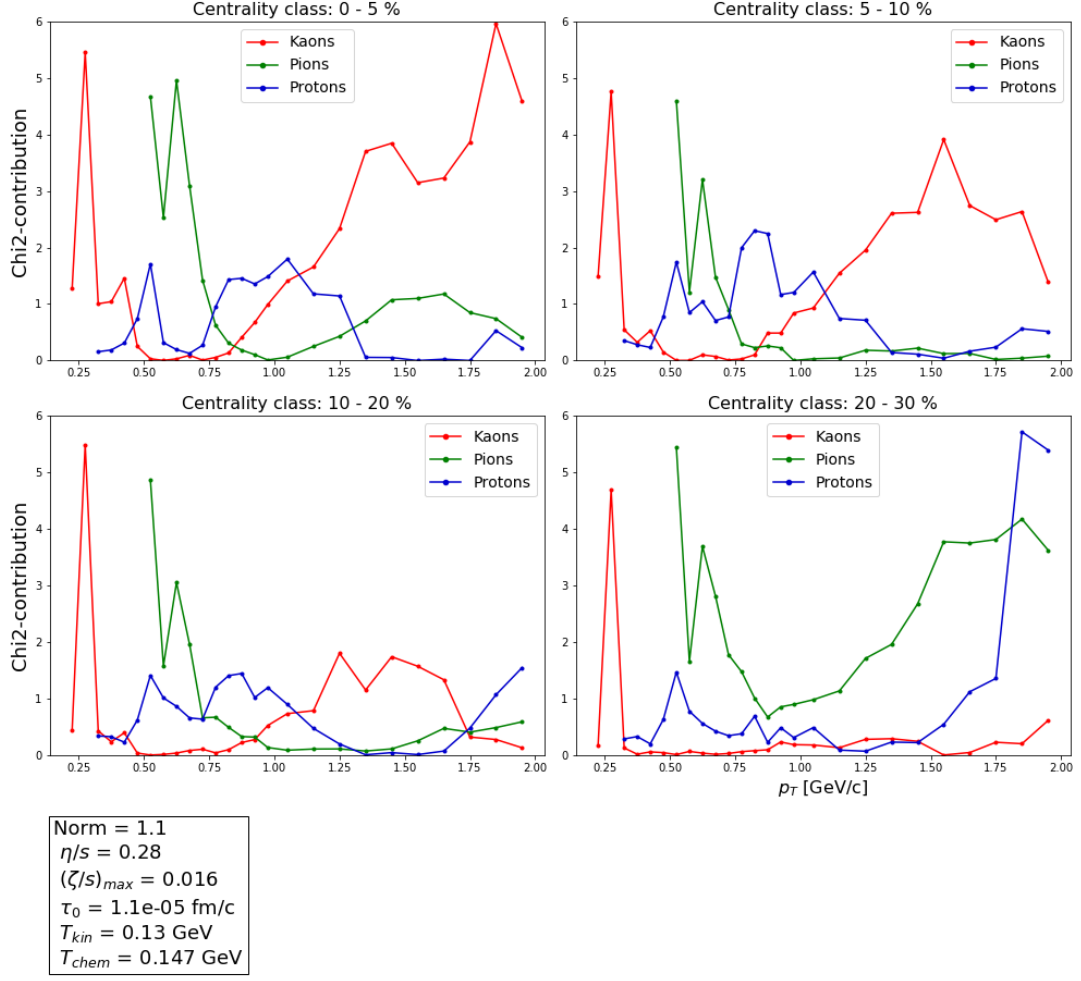


Figure 4.9: Contribution to the χ^2 -value for each p_T -interval for the fit to Xe-Xe data at $\sqrt{s_{NN}} = 5.44$ TeV for four centrality classes and p_T -values up to 2 GeV/c.

4.3.3 Five centrality classes and p_T -values up to 2 GeV

Finally, to get a comparison between the impact of excluding high- p_T values and excluding the 30-40% centrality class, the same procedure is repeated for five centrality classes, but excluded p_T -values above 2 GeV/c.

The best fitting parameters in this case are the following:

- norm: 1.3
- shear viscosity over entropy ratio η/s : 0.288
- maximum of the bulk viscosity over entropy ratio $(\zeta/s)_{max}$: 0.016
- thermalisation time τ_0 : $1.4 \cdot 10^{-5}$ fm/c

- kinetic freeze-out temperature T_{kin} : 132 MeV
- chemical freeze-out temperature T_{chem} : 147 MeV

The χ^2 -value results to be $\chi^2 = 452.28$ and the number of degrees of freedom is $N_{\text{dof}} = 344$, so the reduced χ^2 -value is $\chi_{\text{red}}^2 = 1.31$.

This is of the same scale as the χ_{red}^2 -value of the fit for the four centrality classes and p_T -values up to 3 GeV/c, which was $\chi_{\text{red}}^2 = 1.33$ (compare section 4.3.1 on page 37). So for the fitting in this grid of parameters, the p_T -values above 2 GeV/c have a similar impact on the χ_{red}^2 -value as the 30-40%-centrality class.

4.4 Comparison of the different fitting ranges

The fit values found in these four different scenarios, each for a different fitting range, are reported together with their resulting χ_{red}^2 in table 4.3.

p_T -range \leq	3 GeV/c	3 GeV/c	2 GeV/c	2 GeV/c
# centrality classes	5	4	4	5
norm	1.3	1.5	1.1	1.3
η/s	0.28	0.28	0.28	0.288
$(\zeta/s)_{\text{max}}$	0.0144	0.016	0.016	0.016
τ_0 [fm/c]	$1.1 \cdot 10^{-5}$	$1.7 \cdot 10^{-5}$	$1.1 \cdot 10^{-5}$	$1.4 \cdot 10^{-5}$
T_{kin} [MeV]	136	134	130	132
T_{chem} [MeV]	147.5	147	147	147
χ_{red}^2	1.64	1.33	1.12	1.31

Table 4.3: Results for the parameters and their according goodness of fit for different fitting ranges.

Some parameters seem to be quite stable towards the variation of fitting ranges. These are for example the viscosities; the shear viscosity over entropy ratio η/s is 0.28 in all cases besides the last one, where it slightly increased to 0.288, and the maximum of the bulk viscosity over entropy ratio $(\zeta/s)_{\text{max}}$ is 0.016 in all cases besides the first one, where it is with a value of 0.0144 slightly lower.

The chemical freeze-out temperature is stable as well with a value of 147.5 MeV in the first column of table 4.3 and a value of 147 MeV in the three other cases.

On the other side, the parameters norm, τ_0 and T_{kin} fluctuate a lot within the grid for the different fitting scenarios. Although no error estimation has been done so far, large fluctuations are indicative of large uncertainties. Therefore it can be argued

that the parameters η/s , $(\zeta/s)_{\max}$ and T_{chem} can be determined more precisely than the parameters τ_0 and T_{kin} .

The chosen grid ranges reported in table 4.2 also heavily influence the results obtained in this analysis and should be commented. For example, for the chemical freeze-out temperature a range between 146.5 MeV and 149 MeV was set. This means that a range of only 2.5 MeV is covered for the chemical freeze-out parameter. For the kinetic freeze-out temperature, the grid contains values between 130 MeV and 140 MeV, so the span between upper and lower limit is with 10 MeV four times as large as the span of the upper and lower limit of the chemical freeze-out temperature. This observation indicates once more that the chemical freeze-out temperature was determined with a higher precision, while for the kinetic freeze-out temperature this seemed to be not as simple.

Moreover, the chosen grid ranges obviously limit the possible results that can be obtained. The 46656 different possible configurations that were compared cover already a large area in the sixdimensional parameter space, but the fact that we can't allow for infinite configurations limits the possibilities. For instance, the true global minimum could lie between the grid points and the discretisation of the grid would then restrict the accuracy of its determination. It could also possibly lie outside the grid ranges and would then never be found. Therefore it is definitely worth a discussion if the obtained values indeed represent the global minimum and if the parameters describe the evolution of the quark-gluon plasma well.

4.5 Discussion of the thermalisation time and the free-streaming approach

Especially the thermalisation time resulted in really small values. The results range between $\tau_0 = 1.1 \cdot 10^{-5}$ fm/c and $\tau_0 = 1.7 \cdot 10^{-5}$ fm/c, as reported in table 4.3. Many papers have indicated to a thermalisation time around 1 fm/c [4, 38, 39]. Previous works with Fluidum have found values ranging between 0.1 fm/c – 0.4 fm/c [11, 36]. Accordingly, the values found in this thesis differ by four orders of magnitude from previous results obtained with Fluidum.

It is quite interesting that Fluidum is able to produce such good fits at such a small thermalisation time. From a physical point of view, it is unrealistic that the thermalisation time is going to zero, because this would mean that the system would be immediately equilibrated after the collision.

There is actually an ongoing discussion about the possible reasons for the differ-

ences between Fluidum calculation and ALICE data suggesting to add a phase of free-streaming expansion before the thermalisation [40, 41]. The issue in Fluidum is that it tends to get as much as possible evolution time to build up the transverse momentum. As a consequence, the thermalisation time is forced towards zero in order to have an earlier fluid dynamic description. The tendency to gain as much as possible hydrodynamic evolution time could not only cause the hydrodynamic description to start earlier, but also to last for a longer time meaning that the freeze-out temperatures would be pushed to lower values.

This problem can be avoided by adding about 1 fm/c of free-streaming to the description of a heavy-ion collision. For this ansatz, the particles are described as non-interacting after the overlap of the nuclei which allows them to build up more fluid velocity in the transverse plane. After a time of 1 fm/c they undergo a sudden equilibration and only from that time on the hydrodynamic description by Fluidum is applied. In contrast to the case without free-streaming where the velocity fields in Fluidum need to build up from zero, the free-streaming approach ensures to have non-zero starting velocity and momentum at the beginning of the Fluidum description. Consequently, adding ~ 1 fm/c of free-streaming significantly improves the description of mean p_T , which is the first momentum of the p_T -distribution, and also values at higher p_T are described better.

As a second effect, free-streaming also smoothens the fluctuations of the initial entropy density distribution. More fluctuations suppress the contribution to the p_T -spectra (and therefore also to the mean p_T) as Fluidum only decomposes the entropy density up to linear order and higher orders and therefore larger fluctuations are not captured.

Implementing a free-streaming expansion phase could therefore avoid the problem of the thermalisation time going to zero and at the same time the underestimation of values at higher p_T could possibly be solved.

Chapter 5

Summary and Outlook

In this thesis, the ability of a hydrodynamic model to describe the production of pions, kaons and protons in xenon-xenon collisions at $\sqrt{s_{\text{NN}}} = 5.44$ TeV at the LHC was investigated. For the hydrodynamic description a combination of the initial condition model "T_RENT_O", the fluid dynamic model "FluiduM" and the freeze-out and resonance decay package "FastReso" was used. In this theoretical model, six parameters were left as free fit parameters, which are the normalisation factor for the entropy density "norm", τ_0 , η/s , $(\zeta/s)_{\text{max}}$, T_{kin} and T_{chem} .

In order to determine these free parameters, Fluidum calculations were performed for an equally-spaced grid in the sixdimensional parameter space with six values in each dimension. With an investigation of the χ^2 -values resulting from the comparison to the ALICE data, the gridpoint with the lowest χ^2 -value was identified as the best fit. For the set of parameters corresponding to the best fit we obtained $\chi_{\text{red}}^2 = 1.64$. By analysing the data-to-model ratios and the χ^2 -contributions per p_T -interval and per centrality class, it was found that especially values at high p_T and for peripheral collisions are not described appropriately by the hydrodynamic model and contribute highly to the χ^2 -value.

By only excluding the 30-40% centrality class, the fit could be improved to $\chi_{\text{red}}^2 = 1.33$ and when only excluding the p_T -range from 2 GeV/c to 3 GeV/c, the fit could be improved to $\chi_{\text{red}}^2 = 1.31$.

When excluding both the 30-40% centrality class and $p_T \geq 2$ GeV/c, the fit improved to $\chi_{\text{red}}^2 = 1.12$.

Along the way, results for the six parameters were presented. Nevertheless, we could not constrain all six parameters to narrow ranges. Especially the thermalisation time τ_0 resulted to be significantly smaller compared to results obtained in previous works.

At this point the addition of a free-streaming expansion phase between the time of collision and the thermalisation time seems very promising. It could circumvent the problem of the thermalisation time going to zero and allow for a better description of the particle spectra overall, but especially at higher p_T .

Additionally further grid ranges should be investigated, possibly also with a higher granularity, to clarify the question if there might be other local minima at different locations of the parameter space. One approach to optimise the time and computing power consuming grid search would be to use a Latin hypercube sampling instead of a regular grid. This way the particle spectra for wider parameter ranges could be calculated without inflating the computing power needed too much. Furthermore, approaches on improving the fitting procedure with the help of a Neural Network are already in discussion and promise faster and more precise results in the future.

Bibliography

- [1] *Standard Model of Elementary Particles*. Sept. 17, 2019. URL: https://en.wikipedia.org/wiki/File:Standard_Model_of_Elementary_Particles.svg (visited on 10/10/2022) (cited on page 2).
- [2] Alexandre Deur, Stanley J. Brodsky, and Guy F. de Téramond. “The QCD running coupling”. In: *Progress in Particle and Nuclear Physics* 90 (2016), pp. 1–10. ISSN: 0146-6410. DOI: <https://doi.org/10.1016/j.pnnp.2016.04.003>. URL: <https://www.sciencedirect.com/science/article/pii/S0146641016300035> (cited on page 3).
- [3] P.A. Zyla et al. “Review of Particle Physics”. In: *PTEP* 2020.8 (2020). and 2021 update, Chapter 9: Quantum Chromodynamics, Figure 9.3, p. 167. DOI: [10.1093/ptep/ptaa104](https://doi.org/10.1093/ptep/ptaa104) (cited on page 3).
- [4] Rajeev S. Bhalerao. “Relativistic heavy-ion collisions”. In: *K. Kawagoe, M. Mulders: 1st Asia-Europe-Pacific School of High-Energy Physics* (2014), pp. 219–239. CERN Yellow Reports: School Proceedings. CERN–2014–001, KEK–Proceedings–2013–8. Geneva: CERN. ISSN: 0531–4283. DOI: [10.5170/CERN-2014-001](https://doi.org/10.5170/CERN-2014-001). URL: <http://cds.cern.ch/record/1443909> (cited on pages 4–6, 43).
- [5] C.G. Wohl. *Particle Data Group: Physical Constants*. 2019. URL: <https://pdg.lbl.gov/2021/reviews/rpp2020-rev-phys-constants.pdf> (visited on 10/14/2022) (cited on pages 4, 5, 8).
- [6] Reinhard Stock. “7 Relativistic Nucleus-Nucleus Collisions and the QCD Matter Phase Diagram”. In: *Landolt-Börnstein - Group I Elementary Particles, Nuclei and Atoms* (2008), p. 39. ISSN: 1616-9522. DOI: [10.1007/978-3-540-74203-6_7](https://doi.org/10.1007/978-3-540-74203-6_7). arXiv: 0807.1610 [hep-th]. URL: http://dx.doi.org/10.1007/978-3-540-74203-6_7 (cited on page 7).

- [7] A. Bazavov et al. “Chiral crossover in QCD at zero and non-zero chemical potentials”. In: *Physics Letters B* 795 (2019), pp. 15–21. ISSN: 0370-2693. DOI: <https://doi.org/10.1016/j.physletb.2019.05.013>. URL: <https://www.sciencedirect.com/science/article/pii/S0370269319303223> (cited on page 6).
- [8] Patrick Steinbrecher. “The QCD crossover at zero and non-zero baryon densities from Lattice QCD”. In: *Nuclear Physics A* 982 (2019). The 27th International Conference on Ultrarelativistic Nucleus-Nucleus Collisions: Quark Matter 2018, pp. 847–850. ISSN: 0375-9474. DOI: <https://doi.org/10.1016/j.nuclphysa.2018.08.025>. URL: <https://www.sciencedirect.com/science/article/pii/S0375947418301696> (cited on page 6).
- [9] Charles Gale et al. *Event-plane decorrelation of photons produced in the early stage of heavy-ion collisions*. 2020. DOI: 10.48550/ARXIV.2009.07841. URL: <https://arxiv.org/abs/2009.07841> (cited on pages 7, 8).
- [10] Chun Shen et al. *The iEBE-VISHNU code package for relativistic heavy-ion collisions*. 2014. DOI: 10.48550/ARXIV.1409.8164. URL: <https://arxiv.org/abs/1409.8164> (cited on pages 7, 8).
- [11] Christian Sonnabend. “On the influence of temperature-dependent η/s on transverse-momentum particle spectra in heavy-ion collisions”. In: (Oct. 2020). URL: https://www.physi.uni-heidelberg.de/Publications/ChristianSonnabend_BachelorThesis.pdf (visited on 10/17/2022) (cited on pages 7, 8, 25, 27, 29, 34, 43).
- [12] *The Large Hadron Collider*. URL: <https://home.cern/science/accelerators/large-hadron-collider> (visited on 10/20/2022) (cited on pages 9, 10).
- [13] *The CERN accelerator complex*. URL: <https://cds.cern.ch/record/2693837/files/Poster-2019-858.pdf> (visited on 10/20/2022) (cited on page 9).
- [14] “One of the first Xenon-Xenon collisions at LHC registered by ALICE”. In: (Oct. 13, 2017). URL: <https://cds.cern.ch/record/2289018/> (visited on 10/26/2022) (cited on page 10).
- [15] *Schematics of the ALICE subdetectors*. Feb. 27, 2014. URL: [https://commons.wikimedia.org/wiki/File:2012-Aug-02-ALICE_3D_v0_with_Text_\(1\)_2.jpg](https://commons.wikimedia.org/wiki/File:2012-Aug-02-ALICE_3D_v0_with_Text_(1)_2.jpg) (visited on 10/21/2022) (cited on pages 10, 19).

BIBLIOGRAPHY

- [16] E. Scapparone. “Particle identification with the ALICE detector”. In: *Nuclear Instruments and Methods in Physics Research Section A: Accelerators, Spectrometers, Detectors and Associated Equipment* 598.1 (2009). Instrumentation for Colliding Beam Physics, pp. 152–155. ISSN: 0168-9002. DOI: <https://doi.org/10.1016/j.nima.2008.08.074>. URL: <https://www.sciencedirect.com/science/article/pii/S0168900208012138> (cited on pages 11, 12).
- [17] P. Antonioli. “The ALICE time of flight system”. In: *Nuclear Physics B - Proceedings Supplements* 125 (2003). Innovative Particle and Radiation Detectors, pp. 193–197. ISSN: 0920-5632. DOI: [https://doi.org/10.1016/S0920-5632\(03\)90990-X](https://doi.org/10.1016/S0920-5632(03)90990-X). URL: <https://www.sciencedirect.com/science/article/pii/S092056320390990X> (cited on page 11).
- [18] A. Alici. “The MRPC-based ALICE time-of-flight detector: Status and performance”. In: *Nuclear Instruments and Methods in Physics Research Section A: Accelerators, Spectrometers, Detectors and Associated Equipment* 706 (2013). TRDs for the Third Millenium, pp. 29–32. ISSN: 0168-9002. DOI: <https://doi.org/10.1016/j.nima.2012.05.004>. URL: <https://www.sciencedirect.com/science/article/pii/S0168900212004755> (cited on page 12).
- [19] *ALICE HMPID*. URL: <https://alice-collaboration.web.cern.ch/node/34963> (visited on 10/19/2022) (cited on page 12).
- [20] *ALICE TRD*. URL: https://alice-collaboration.web.cern.ch/menu_proj_items/trd (visited on 10/19/2022) (cited on page 12).
- [21] *ALICE EMCAL*. URL: https://alice-collaboration.web.cern.ch/menu_proj_items/emcal (visited on 10/19/2022) (cited on page 12).
- [22] *ALICE PHOS*. URL: <https://alice-collaboration.web.cern.ch/node/34980> (visited on 10/19/2022) (cited on page 12).
- [23] *ALICE Muon spectrometer*. URL: <https://alice-collaboration.web.cern.ch/node/34983> (visited on 10/19/2022) (cited on page 12).
- [24] *Official website of the ALICE experiment*. URL: <https://alice.cern/#experiment> (visited on 10/19/2022) (cited on page 12).
- [25] ALICE Collaboration. *Production of pions, kaons, (anti-)protons and ϕ mesons in Xe-Xe collisions at $\sqrt{s_{NN}} = 5.44$ TeV*. 2021. arXiv: 2101.03100 [nucl-ex] (cited on pages 12, 13, 15).

-
- [26] Michael L. Miller et al. “Glauber Modeling in High-Energy Nuclear Collisions”. In: *Annual Review of Nuclear and Particle Science* 57.1 (2007), pp. 211–217. DOI: 10.1146/annurev.nucl.57.090506.123020. eprint: <https://doi.org/10.1146/annurev.nucl.57.090506.123020>. URL: <https://doi.org/10.1146/annurev.nucl.57.090506.123020> (cited on pages 14, 20, 21, 23).
- [27] ALICE Collaboration. *Production of pions, kaons, (anti-)protons and ϕ mesons in Xe–Xe collisions at $\sqrt{s_{NN}} = 5.44$ TeV*. HEPData (collection). <https://doi.org/10.17182/hepdata.110161>. 2021 (cited on pages 15, 16, 29).
- [28] *Periodic table*. Nov. 3, 2022. URL: https://en.wikipedia.org/wiki/Periodic_table (visited on 11/03/2022) (cited on page 15).
- [29] Stefan Floerchinger, Eduardo Grossi, and Jorrit Lion. “Fluid dynamics of heavy ion collisions with mode expansion”. In: *Physical Review C* 100.1 (2019). ISSN: 2469-9993. DOI: 10.1103/physrevc.100.014905. URL: <http://dx.doi.org/10.1103/PhysRevC.100.014905> (cited on pages 18, 23–25).
- [30] J. Scott Moreland, Jonah E. Bernhard, and Steffen A. Bass. “Alternative ansatz to wounded nucleon and binary collision scaling in high-energy nuclear collisions”. In: *Phys. Rev. C* 92 (1 2015), p. 011901. DOI: 10.1103/PhysRevC.92.011901. URL: <https://link.aps.org/doi/10.1103/PhysRevC.92.011901> (cited on pages 18, 22, 23).
- [31] Aleksas Mazeliauskas et al. “Fast resonance decays in nuclear collisions”. In: *The European Physical Journal C* 79.3 (2019). DOI: 10.1140/epjc/s10052-019-6791-7. URL: <https://doi.org/10.1140/epjc/s10052-019-6791-7> (cited on pages 18, 26).
- [32] P. Chochula L. Betev. *Definition of the ALICE Coordinate System and Basic Rules for Subdetector Components Numbering*. Oct. 3, 2003. URL: <http://personalpages.to.infn.it/~tosello/EngMeet/NamingConventions/ALICE-INT-2003-038.pdf> (visited on 11/04/2022) (cited on pages 18, 19).
- [33] Sarah Görlitz. “Impact of initial conditions on integrated particle yields from Pb–Pb collisions at $\sqrt{s_{NN}} = 2.76$ TeV and 5.02 TeV”. In: (Nov. 2020). URL: https://www.physi.uni-heidelberg.de/Publications/Bachelorthesis_Goerlitz.pdf (visited on 10/20/2022) (cited on pages 21, 23).
- [34] Charles Gale, Sangyong Jeon, and Björn Schenke. “Hydrodynamic Modeling of Heavy-Ion Collisions”. In: *International Journal of Modern Physics A* 28.11 (2013), pp. 1–13. ISSN: 1793-656X. DOI: 10.1142/s0217751x13400113. arXiv:

BIBLIOGRAPHY

- 1301.5893 [nucl-th]. URL: <http://dx.doi.org/10.1142/S0217751X13400113> (cited on page 25).
- [35] J. Scott Moreland, Jonah E. Bernhard, and Steffen A. Bass. “Estimating initial state and quark-gluon plasma medium properties using a hybrid model with nucleon substructure calibrated to p-Pb and Pb-Pb collisions at $\sqrt{s_{\text{NN}}} = 5.02$ TeV”. In: *Physical Review C* 101.2 (2020). DOI: 10.1103/physrevc.101.024911. URL: <https://doi.org/10.1103/physrevc.101.024911> (cited on page 25).
- [36] D. Devetak et al. “Global fluid fits to identified particle transverse momentum spectra from heavy-ion collisions at the Large Hadron Collider”. In: *Journal of High Energy Physics* 2020.6 (2020). arXiv: 1909.10485 [hep-ph]. URL: <https://doi.org/10.48550/arXiv.1909.10485> (cited on pages 25–27, 43).
- [37] *Green Cube - Helmholtz Forschungsakademie Hessen für FAIR*. URL: <https://hfhf-hessen.de/en/blog/technologie/green-cube/> (visited on 11/03/2022) (cited on page 28).
- [38] Georg Wolschin. “Aspects of Relativistic Heavy-Ion Collisions”. In: *Universe* 6.5 (2020), p. 61. DOI: 10.3390/universe6050061. URL: <https://doi.org/10.3390/universe6050061> (cited on pages 6, 43).
- [39] Li Yan. “Hydrodynamic modeling of heavy-ion collisions”. In: *Nuclear Physics A* 967 (2017), pp. 89–96. DOI: 10.1016/j.nuclphysa.2017.04.022. URL: <https://doi.org/10.1016/j.nuclphysa.2017.04.022> (cited on pages 6, 43).
- [40] Wojciech Broniowski et al. “Free-streaming approximation in early dynamics of relativistic heavy-ion collisions”. In: *Phys. Rev. C* 80 (2009), p. 034902. DOI: 10.1103/PhysRevC.80.034902. arXiv: 0812.3393 [nucl-th] (cited on page 44).
- [41] Jia Liu, Chun Shen, and Ulrich Heinz. “Pre-equilibrium evolution effects on heavy-ion collision observables”. In: *Phys. Rev. C* 91.6 (2015). [Erratum: *Phys.Rev.C* 92, 049904 (2015)], p. 064906. DOI: 10.1103/PhysRevC.91.064906. arXiv: 1504.02160 [nucl-th] (cited on page 44).

Acknowledgements

First of all, I want to express my gratitude to Silvia Masciocchi for integrating me into her group and especially for giving me the unique opportunity to visit the GSI Helmholtz Centre for Heavy Ion Research and the ALICE detector at CERN in person. Whenever there were issues to discuss, I could rely on her deep understanding, both professionally and humanly.

Furthermore, I want to thank the Isoquant-team for the discussions and inspirations which were a great help. An explicit thanks goes to Andrea Dubla for supporting me all the way and to him and Federica Capellino for proofreading individual chapters. Thank you to Ilya Selyuzhenkov for proofreading the final thesis and to Klaus Reygers for kindly confirming to take over the second assessment.

Finally I would like to thank everyone who is not named here, but who supported me during this time. I am mainly thinking here of all the other current bachelor students in this group with whom I have shared so much suffering as well as good times and from whom I have reaped so much emotional support.

Most of all, I thank my parents for their endless love and support in every possible way throughout my studies and always since. I would never have made it here without you.

Declaration

I declare that this thesis has been composed solely by myself and that it has not been submitted, in whole or in part, in any previous application for a degree. Except where states otherwise by reference or acknowledgement, the work presented is entirely my own.

Heidelberg, December 21, 2022

Franziska Masuch